

On the Geometry of Adversarial Examples

Marc Khoury *
University of California, Berkeley

Dylan Hadfield-Menell †
University of California, Berkeley

December 13, 2018

Abstract

Adversarial examples are a pervasive phenomenon of machine learning models where seemingly imperceptible perturbations to the input lead to misclassifications for otherwise statistically accurate models. We propose a geometric framework, drawing on tools from the manifold reconstruction literature, to analyze the high-dimensional geometry of adversarial examples. In particular, we highlight the importance of *codimension*: for low-dimensional data manifolds embedded in high-dimensional space there are many directions off the manifold in which to construct adversarial examples. Adversarial examples are a natural consequence of learning a decision boundary that classifies the low-dimensional data manifold well, but classifies points near the manifold incorrectly. Using our geometric framework we prove (1) a tradeoff between robustness under different norms, (2) that adversarial training in balls around the data is sample inefficient, and (3) sufficient sampling conditions under which nearest neighbor classifiers and ball-based adversarial training are robust.

keywords: adversarial examples, high-dimensional geometry, robustness, generalization

arXiv:1811.00525v2 [cs.LG] 11 Dec 2018

*khoury@eecs.berkeley.edu

†dhm@eecs.berkeley.edu

1 Introduction

Deep learning at scale has led to breakthroughs on important problems in computer vision (Krizhevsky et al. (2012)), natural language processing (Wu et al. (2016)), and robotics (Levine et al. (2015)). Shortly thereafter, the interesting phenomena of *adversarial examples* was observed. A seemingly ubiquitous property of machine learning models where perturbations of the input that are imperceptible to humans reliably lead to confident incorrect classifications (Szegedy et al. (2013); Goodfellow et al. (2014)). What has ensued is a standard story from the security literature: a game of cat and mouse where defenses are proposed only to be quickly defeated by stronger attacks (Athalye et al. (2018)). This has led researchers to develop methods which are provably robust under specific attack models (Madry et al. (2018); Wong and Kolter (2018); Sinha et al. (2018); Raghunathan et al. (2018)). As machine learning proliferates into society, including security-critical settings like health care (Esteva et al. (2017)) or autonomous vehicles (Codevilla et al. (2018)), it is crucial to develop methods that allow us to understand the vulnerability of our models and design appropriate counter-measures.

In this paper, we propose a geometric framework for analyzing the phenomenon of adversarial examples. We leverage the observation that datasets encountered in practice exhibit low-dimensional structure despite being embedded in very high-dimensional input spaces. This property is colloquially referred to as the “Manifold Hypothesis”: the idea that low-dimensional structure of ‘real’ data leads to tractable learning. We model data as being sampled from class-specific low-dimensional manifolds embedded in a high-dimensional space. We consider a threat model where an adversary may choose *any* point on the data manifold to perturb by ϵ in order to fool a classifier. In order to be robust to such an adversary, a classifier must be correct everywhere in an ϵ -tube around the data manifold. Observe that, even though the data manifold is a low-dimensional object, this tube has the same dimension as the entire space the manifold is embedded in. Our analysis argues that adversarial examples are a natural consequence of learning a decision boundary that classifies all points on a low-dimensional data manifold correctly, but classifies many points near the manifold incorrectly. The high *codimension*, the difference between the dimension of the data manifold and the dimension of the embedding space, is a key source of the pervasiveness of adversarial examples.

Our paper makes the following contributions. First, we develop a geometric framework, inspired by the manifold reconstruction literature, that formalizes the manifold hypothesis described above and our attack model. Second, we highlight the role *codimension* plays in vulnerability to adversarial examples. As the codimension increases, there are an increasing number of directions off the data manifold in which to construct adversarial perturbations. Prior work has attributed vulnerability to adversarial examples to input dimension (Gilmer et al. (2018)). This is the first work that investigates the role of *codimension* in adversarial examples. Interestingly, we find that different classification algorithms are less sensitive to changes in codimension. Third, we apply this framework to prove the following results: (1) we show that the choice of norm to restrict an adversary is important in that there exists a tradeoff between being robust to different norms: we present a classification problem where improving robustness under the $\|\cdot\|_\infty$ norm requires a loss of $\Omega(1 - 1/\sqrt{d})$ in robustness to the $\|\cdot\|_2$ norm; (2) we show that a common approach, training against adversarial examples drawn from balls around the training set, is insufficient to learn robust decision boundaries with realistic amounts of data; and (3) we show that nearest neighbor classifiers do not suffer from this insufficiency, due to geometric properties of their decision boundary away from data, and thus represent a potentially robust classification algorithm. Finally we provide experimental evidence on synthetic datasets and MNIST that support our theoretical results.

2 Related Work

This paper approaches the problem of adversarial examples using techniques and intuition from the manifold reconstruction literature. Both fields have a great deal of prior work, so we focus on only the most related papers here.

2.1 Adversarial Examples

Some previous work has considered the relationships between adversarial examples and high dimensional geometry. Franceschi et al. (2018) explore the robustness of classifiers to random noise in terms of distance to the decision boundary, under the assumption that the decision boundary is locally flat. The work of Gilmer et al. (2018) experimentally evaluated the setting of two concentric under-sampled 499-spheres embedded in \mathbb{R}^{500} , and concluded that adversarial examples occur on the data manifold. In contrast, we present a geometric framework for proving robustness guarantees for learning algorithms, that makes no assumptions on the decision boundary. We carefully sample the data manifold in order to highlight the importance of *codimension*; adversarial examples

exist *even* when the manifold is perfectly classified. Additionally we explore the importance of the spacing between the constituent data manifolds, sampling requirements for learning algorithms, and the relationship between model complexity and robustness.

Wang et al. (2018) explore the robustness of k -nearest neighbor classifiers to adversarial examples. In the setting where the Bayes optimal classifier is uncertain about the true label of each point, they show that k -nearest neighbors is not robust if k is a small constant. They also show that if $k \in \Omega(\sqrt{dn \log n})$, then k -nearest neighbors is robust. Using our geometric framework we show a complementary result: in the setting where each point is certain of its label, 1-nearest neighbors is robust to adversarial examples.

The decision and medial axes defined in Section 3 are maximum margin decision boundaries. Hard margin SVMs define a linear separator with maximum margin, maximum distance from the training data (Cortes and Vapnik (1995)). Kernel methods allow for maximum margin decision boundaries that are non-linear by using additional features to project the data into a higher-dimensional feature space (Shawe-Taylor and Cristianini (2004)). The decision and medial axes generalize the notion of maximum margin to account for the arbitrary curvature of the data manifolds. There have been attempts to incorporate maximum margins into deep learning (Sun et al. (2016); Liu et al. (2016); Liang et al. (2017); Elsayed et al. (2018)), often by designing loss functions that encourage large margins at either the output (Sun et al. (2016)) or at any layer (Elsayed et al. (2018)). In contrast, the decision axis is defined on the input space and we use it as an analysis tool for proving robustness guarantees.

2.2 Manifold Reconstruction

Manifold reconstruction is the problem of discovering the structure of a k -dimensional manifold embedded in \mathbb{R}^d , given *only* a set of points sampled from the manifold. A large vein of research in manifold reconstruction develops algorithms that are *provably good*: if the points sampled from the underlying manifold are sufficiently dense, these algorithms are guaranteed to produce a geometrically accurate representation of the unknown manifold with the correct topology. The output of these algorithms is often a *simplicial complex*, a set of simplices such as triangles, tetrahedra, and higher-dimensional variants, that approximate the unknown manifold. In particular these algorithms output subsets of the Delaunay triangulation, which along with their geometric dual the Voronoi diagram, have properties that aid in proving geometric and topological guarantees (Edelsbrunner and Shah (1997)).

The field first focused on curve reconstruction in \mathbb{R}^2 (Amenta et al. (1998)) and subsequently in \mathbb{R}^3 (Dey and Kumar (1999)). Soon after algorithms were developed for surface reconstruction in \mathbb{R}^3 , both in the noise-free setting (Amenta and Bern (1999); Amenta et al. (2002)) and in the presence of noise (Dey and Goswami (2004)). We borrow heavily from the analysis tools of these early works, including the medial axis and the reach. However we emphasize that we have adapted these tools to the learning setting. To the best of our knowledge, our work is the first to consider the medial axis under different norms.

In higher-dimensional embedding spaces (large d), manifold reconstruction algorithms face the *curse of dimensionality*. In particular, the Delaunay triangulation, which forms the bedrock of algorithms in low-dimensions, of n vertices in \mathbb{R}^d can have up to $\Theta(n^{\lceil d/2 \rceil})$ simplices. To circumvent the curse of dimensionality, algorithms were proposed that compute subsets of the Delaunay triangulation restricted to the k -dimensional tangent spaces of the manifold at each sample point (Boissonnat and Ghosh (2014)). Unfortunately, progress on higher-dimensional manifolds has been limited due to the presence of so-called “sliver” simplices, poorly shaped simplices that cause in-consistencies between the local triangulations constructed in each tangent space (Cheng et al. (2005); Boissonnat and Ghosh (2014)). Techniques that provably remove sliver simplices have prohibitive sampling requirements (Cheng et al. (2000); Boissonnat and Ghosh (2014)). Even in the special case of surfaces ($k = 2$) embedded in high dimensions ($d > 3$), algorithms with practical sampling requirements have only recently been proposed (Khoury and Shewchuk (2016)). Our use of tubular neighborhoods as a tool for analysis is borrowed from Dey et al. (2005) and Khoury and Shewchuk (2016).

In this paper we are interested in *learning* robust decision boundaries, *not* reconstructing the underlying data manifolds, and so we avoid the use of Delaunay triangulations and their difficulties entirely. In Section 5 we present robustness guarantees for two learning algorithms in terms of a sampling condition on the underlying manifold. These sampling requirements scale with the dimension of the underlying manifold k , *not* with the dimension of the embedding space d .

3 The Geometry of Data

We model data as being sampled from a set of low-dimensional manifolds (with or without boundary) embedded in a high-dimensional space \mathbb{R}^d . We use k to denote the dimension of a manifold $\mathcal{M} \subset \mathbb{R}^d$. The special case of a 1-manifold is called a *curve*, and a 2-manifold is a *surface*. The *codimension* of \mathcal{M} is $d - k$, the difference

between the dimension of the manifold and the dimension of the embedding space. The ‘‘Manifold Hypothesis’’ is the observation that in practice, data is often sampled from manifolds, usually of high codimension.

In this paper we are primarily interested in the classification problem. Thus we model data as being sampled from C class manifolds $\mathcal{M}_1, \dots, \mathcal{M}_C$, one for each class. When we wish to refer to the entire space from which a dataset is sampled, we refer to the *data manifold* $\mathcal{M} = \cup_{1 \leq j \leq C} \mathcal{M}_j$. We often work with a finite sample of n points, $X \subset \mathcal{M}$, and we write $X = \{X_1, X_2, \dots, X_n\}$. Each sample point X_i has an accompanying class label $y_i \in \{1, 2, \dots, C\}$ indicating which manifold \mathcal{M}_{y_i} the point X_i is sampled from.

Consider a $\|\cdot\|_p$ -ball B centered at some point $c \in \mathbb{R}^d$ and imagine growing B by increasing its radius starting from zero. For nearly all starting points c , the ball B eventually intersects one, and only one, of the \mathcal{M}_i ’s. Thus the nearest point to c on \mathcal{M} , in the norm $\|\cdot\|_p$, lies on \mathcal{M}_i . (Note that the nearest point on \mathcal{M}_i need not be unique.)

The *decision axis* Λ_p of \mathcal{M} is the set of points c such that the boundary of B intersects two or more of the \mathcal{M}_i , but the interior of B does not intersect \mathcal{M} at all. In other words, the decision axis Λ_p is the set of points that have two or more closest points, in the norm $\|\cdot\|_p$, on distinct class manifolds. See Figure 1. The decision axis is inspired by the medial axis, which was first proposed by Blum (1967) in the context of image analysis and subsequently modified for the purposes of curve and surface reconstruction by Amenta et al. (1998; 2002). We have modified the definition to account for multiple class manifolds and have renamed our variant in order to avoid confusion in the future.

The decision axis Λ_p can intuitively be thought of as a decision boundary that is optimal in the following sense. First, Λ_p separates the class manifolds when they do not intersect (Lemma 8). Second, each point of Λ_p is as far away from the class manifolds as possible in the norm $\|\cdot\|_p$. As shown in the leftmost example in Figure 1, in the case of two linearly separable circles of equal radius, the decision axis Λ_2 is exactly the line that separates the data with maximum margin. For arbitrary manifolds, Λ_p generalizes the notion of maximum margin to account for the arbitrary curvature of the class manifolds.

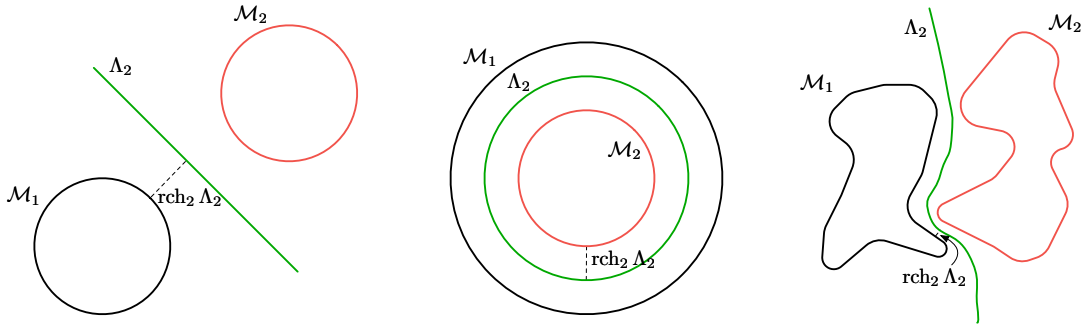


Figure 1: Examples of the decision axis Λ_2 , shown here in green, for different data manifolds. Intuitively, the decision axis captures an optimal decision boundary between the data manifolds. It’s optimal in the sense that each point on the decision axis is as far away from each data manifold as possible. Notice that in the first example, the decision axis coincides with the maximum margin line.

Let $T \subset \mathbb{R}^d$ be any set. The *reach* $\text{rch}_p(T; \mathcal{M})$ of \mathcal{M} is defined as $\inf_{x \in \mathcal{M}, y \in T} \|x - y\|_p$. When \mathcal{M} is compact, the reach is achieved by the point on \mathcal{M} that is closest to T under the $\|\cdot\|_p$ norm. We will drop \mathcal{M} from the notation when it is understood from context.

Finally, an ϵ -*tubular neighborhood* of \mathcal{M} is defined as $\mathcal{M}^{\epsilon, p} = \{x \in \mathbb{R}^d : \inf_{y \in \mathcal{M}} \|x - y\|_p \leq \epsilon\}$. That is, $\mathcal{M}^{\epsilon, p}$ is the set of all points whose distance to \mathcal{M} under the metric induced by $\|\cdot\|_p$ is less than ϵ . Note that while \mathcal{M} is k -dimensional, $\mathcal{M}^{\epsilon, p}$ is always d -dimensional. Tubular neighborhoods are how we rigorously define adversarial examples. Consider a classifier $f : \mathbb{R}^d \rightarrow [C]$ for \mathcal{M} . An ϵ -*adversarial example* is a point $x \in \mathcal{M}_i^{\epsilon, p}$ such that $f(x) \neq i$. A classifier f is robust to all ϵ -adversarial examples when f correctly classifies not only \mathcal{M} , but all of $\mathcal{M}^{\epsilon, p}$. Thus the problem of being robust to adversarial examples is rightly seen as one of *generalization*. In this paper we will be primarily concerned with exploring the conditions under which we can provably learn a decision boundary that correctly classifies $\mathcal{M}^{\epsilon, p}$. When $\epsilon < \text{rch}_p \Lambda_p$, the decision axis Λ_p is one decision boundary that correctly classifies $\mathcal{M}^{\epsilon, p}$ (Corollary 10). Throughout the remainder of the paper we will drop the p in $\mathcal{M}^{\epsilon, p}$ from the notation, instead writing \mathcal{M}^ϵ ; the norm will always be clear from context.

The geometric quantities defined above can be defined more generally for any distance metric $d(\cdot, \cdot)$. In this paper we will focus exclusively on the metrics induced by the norms $\|\cdot\|_p$ for $p > 0$. The decision axis under $\|\cdot\|_2$ is in general *not* identical to the decision axis under $\|\cdot\|_\infty$. In Section 4 we will prove that since Λ_2 is not identical to Λ_∞ there exists a tradeoff in the robustness of any decision boundary between the two norms.

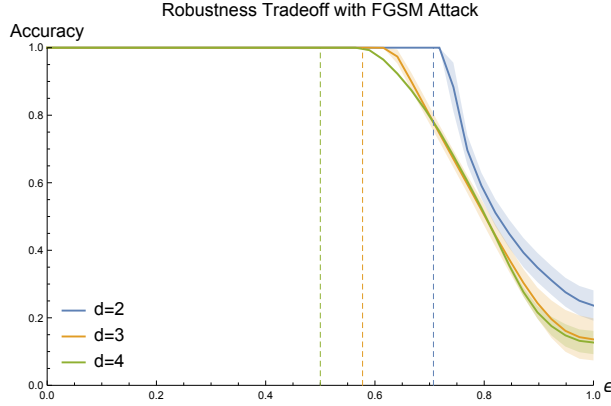


Figure 2: As the dimension increases, the $\text{rch}_2(\Lambda_\infty; S_1 \cup S_2)$ decreases, and so an $\|\cdot\|_\infty$ robust classifier is less robust to $\|\cdot\|_2$ attacks. The dashed lines are placed at $1/\sqrt{d}$, where our theoretical results suggest we should start finding $\|\cdot\|_2$ adversarial examples. We use the robust $\|\cdot\|_\infty$ loss of Wong and Kolter (2018)

4 A Provable Tradeoff in Robustness Between Norms

Schott et al. (2018) explore the vulnerability of robust classifiers to attacks under different norms. In particular, they take the robust pretrained classifier of Madry et al. (2018), which was trained to be robust to $\|\cdot\|_\infty$ -perturbations, and subject it to $\|\cdot\|_0$ and $\|\cdot\|_2$ attacks. They show that accuracy drops to 0% under $\|\cdot\|_0$ attacks and to 35% under $\|\cdot\|_2$. Here we explain why poor robustness under the norm $\|\cdot\|_2$ should be expected.

We say a decision boundary \mathcal{D}_f for a classifier f is ϵ -robust in the $\|\cdot\|_p$ norm if $\epsilon < \text{rch}_p \mathcal{D}_f$. In words, starting from any point $x \in \mathcal{M}$, a perturbation η_x must have p -norm greater than $\text{rch}_p \mathcal{D}_f$ to cross the decision boundary. The most robust decision boundary to $\|\cdot\|_p$ -perturbations is Λ_p . In Theorem 1 we construct a learning setting where Λ_2 is distinct from Λ_∞ . Thus, in general, *no single decision boundary can be optimally robust in all norms*.

Theorem 1. *Let $S_1, S_2 \subset \mathbb{R}^{d+1}$ be two concentric d -spheres with radii $r_1 < r_2$ respectively. Let $S = S_1 \cup S_2$ and let $\Lambda_2, \Lambda_\infty$ be the $\|\cdot\|_2$ and $\|\cdot\|_\infty$ decision axes of S . Then $\Lambda_2 \neq \Lambda_\infty$. Furthermore $\text{rch}_2 \Lambda_\infty \in \mathcal{O}(\text{rch}_2 \Lambda_2 / \sqrt{d})$.*

Proof. The decision axis under $\|\cdot\|_2$, Λ_2 , is just the d -sphere with radius $(r_1 + r_2)/2$. However, Λ_∞ is not identical to Λ_2 in this setting; in fact most Λ_∞ of approaches S_1 as d increases.

The geometry of a $\|\cdot\|_\infty$ -ball B_Δ centered at $m \in \mathbb{R}^d$ with radius Δ is that of a hypercube centered at m with side length 2Δ . To find a point on Λ_∞ we place B_Δ tangent to the north pole q of S_1 so that the corners of B_Δ touch S_2 . The north pole has coordinate representation $q = (0, \dots, 0, r_1)$, the center $m = (0, \dots, 0, r_1 + \Delta)$, and a corner of B_Δ can be expressed as $p = (\Delta, \dots, \Delta, r_1 + 2\Delta)$. Additionally we have the constraint that $\|p\|_2 = r_2$ since $p \in S_2$. Then we can solve for Δ as

$$r_2^2 = \|p\|_2^2 = (d-1)\Delta^2 + (r_1 + 2\Delta)^2 = (d+3)\Delta^2 + 4r_1\Delta + r_1^2;$$

$$\Delta = \frac{-2r_1 + \sqrt{r_1^2 + 3r_2^2 + d(r_2^2 - r_1^2)}}{d+3},$$

where the last step follows from the quadratic formula and the fact that $\Delta > 0$. For fixed r_1, r_2 , the value Δ scales as $\mathcal{O}(1/\sqrt{d})$. It follows that $\text{rch}_2 \Lambda_\infty \in \mathcal{O}(\text{rch}_2 \Lambda_2 / \sqrt{d})$. \square

From Theorem 1 we conclude that the minimum distance from S_1 to Λ_∞ under the $\|\cdot\|_2$ norm is upper bounded as $\text{rch}_2 \Lambda_\infty \in \mathcal{O}(\text{rch}_2 \Lambda_2 / \sqrt{d})$. If a classifier f is trained to learn Λ_∞ , an adversary, starting on S_1 , can construct an $\|\cdot\|_2$ adversarial example for a perturbation as small as $\mathcal{O}(1/\sqrt{d})$. Thus we should expect f to be less robust to $\|\cdot\|_2$ -perturbations. Figure 2 verifies this result experimentally.

We expect that $\Lambda_2 \neq \Lambda_\infty$ is the common case in practice. For example, Theorem 1 extends immediately to concentric cylinders and intertwined tori by considering 2-dimensional planar cross-sections. In general, we expect that $\Lambda_2 \neq \Lambda_\infty$ in situations where a 2-dimensional cross-section with \mathcal{M} has nontrivial curvature.

Theorem 1 is important because, even in recent literature, researchers have attributed this phenomena to overfitting. Schott et al. (2018) state that “the widely recognized and by far most successful defense by Madry et al. (1) *overfits* on the L_∞ metric (its highly susceptible to L_2 and L_0 perturbations)” (emphasis ours). We disagree; the Madry et al. (2018) classifier performed exactly as intended. It learned a decision boundary that is robust under $\|\cdot\|_\infty$, which we have shown is quite different from the most robust decision boundary under $\|\cdot\|_2$.

Interestingly, the proposed models of Schott et al. (2018) also suffer from this tradeoff. Their model ABS has accuracy 80% to $\|\cdot\|_2$ attacks but drops to 8% for $\|\cdot\|_\infty$. Similarly their model ABS Binary has accuracy 77% to $\|\cdot\|_\infty$ attacks but drops to 39% for $\|\cdot\|_2$ attacks.

We reiterate, in general, no single decision boundary can be optimally robust in all norms.

5 Provably Robust Classifiers

Adversarial training, the process of training on adversarial examples generated in a $\|\cdot\|_p$ -ball around the training data, is a very natural approach to constructing robust models (Goodfellow et al. (2014); Madry et al. (2018)). In our notation this corresponds to training on samples drawn from X^ϵ for some ϵ . While natural, we show that there are simple settings where this approach is much less sample-efficient than other classification algorithms, if the *only* guarantee is correctness in X^ϵ .

Define a learning algorithm \mathcal{L} with the property that, given a training set $X \subset \mathcal{M}$ sampled from a manifold \mathcal{M} , \mathcal{L} outputs a model $f_{\mathcal{L}}$ such that for every $x \in X$ with label y , and every $\hat{x} \in B(x, \text{rch}_p \Lambda_p)$, $f_{\mathcal{L}}(\hat{x}) = f_{\mathcal{L}}(x) = y$. Here $B(x, r)$ denotes the ball centered at x of radius r in the relevant norm. That is, \mathcal{L} learns a model that outputs the same label for any $\|\cdot\|_p$ -perturbation of x up to $\text{rch}_p \Lambda_p$ as it outputs for x . \mathcal{L} is our theoretical model of adversarial training (Goodfellow et al. (2014); Madry et al. (2018)). Theorem 2 states that \mathcal{L} is sample inefficient in high codimensions.

Theorem 2. *There exists a classification algorithm \mathcal{A} that, for a particular choice of \mathcal{M} , correctly classifies \mathcal{M}^ϵ using exponentially fewer samples than are required for \mathcal{L} to correctly classify \mathcal{M}^ϵ .*

Theorem 2 follows from Theorems 3 and 4. In Theorems 3 and 4 we will prove that a nearest neighbor classifier f_{nn} is one such classification algorithm. Nearest neighbor classifiers are naturally robust in high codimensions because the Voronoi cells of X are *elongated in the directions normal* to \mathcal{M} when X is dense (Dey (2007)).

Before we state Theorem 3 we must introduce a sampling condition on \mathcal{M} . A δ -cover of a manifold \mathcal{M} in the norm $\|\cdot\|_p$ is a finite set of points X such that for every $x \in \mathcal{M}$ there exists X_i such that $\|x - X_i\|_p \leq \delta$. Theorem 3 gives a sufficient sampling condition for $f_{\mathcal{L}}$ to correctly classify \mathcal{M}^ϵ for all manifolds \mathcal{M} . Theorem 3 also provides a sufficient sampling condition for a nearest neighbor classifier f_{nn} to correctly classify \mathcal{M}^ϵ , which is substantially less dense than that of $f_{\mathcal{L}}$. Thus different classification algorithms have different sampling requirements in high codimensions.

Theorem 3. *Let $\mathcal{M} \subset \mathbb{R}^d$ be a k -dimensional manifold and let $\epsilon < \text{rch}_p \Lambda_p$ for any $p > 0$. Let f_{nn} be a nearest neighbor classifier and let $f_{\mathcal{L}}$ be the output of a learning algorithm \mathcal{L} as described above. Let $X_{\text{nn}}, X_{\mathcal{L}} \subset \mathcal{M}$ denote the training sets for f_{nn} and \mathcal{L} respectively. We have the following sampling guarantees:*

1. *If X_{nn} is a δ -cover for $\delta \leq 2(\text{rch}_p \Lambda_p - \epsilon)$ then f_{nn} correctly classifies \mathcal{M}^ϵ .*
2. *If $X_{\mathcal{L}}$ is a δ -cover for $\delta \leq \text{rch}_p \Lambda_p - \epsilon$ then $f_{\mathcal{L}}$ correctly classifies \mathcal{M}^ϵ .*

Proof. Here we use $d(\cdot, \cdot)$ to denote the metric induced by the $\|\cdot\|_p$ norm. We begin by proving (1). Let $q \in \mathcal{M}^\epsilon$ be any point in \mathcal{M}^ϵ . Suppose without loss of generality that $q \in \mathcal{M}_i^\epsilon$ for some class i . The distance $d(q, \mathcal{M}_j)$ from q to any other data manifold \mathcal{M}_j , and thus any sample on \mathcal{M}_j , is lower bounded by $d(q, \mathcal{M}_j) \geq 2 \text{rch}_p \Lambda_p - \epsilon$. See Figure 3. It is then both necessary and sufficient that there exists a $x \in \mathcal{M}_i$ such that $d(q, x) < 2 \text{rch}_p \Lambda_p - \epsilon$ for $f_{\text{nn}}(q) = i$. (Necessary since a properly placed sample on \mathcal{M}_j can achieve the lower bound on $d(q, \mathcal{M}_j)$.) The distance from q to the nearest sample x on \mathcal{M}_i is $d(q, x) \leq \epsilon + \delta$ for some $\delta > 0$. The question is how large can we allow δ to be and still guarantee that f_{nn} correctly classifies \mathcal{M}^ϵ ? We need

$$d(q, x) \leq \epsilon + \delta \leq 2 \text{rch}_p \Lambda_p - \epsilon \leq d(q, \mathcal{M}_j)$$

which implies that $\delta \leq 2(\text{rch}_p \Lambda_p - \epsilon)$. It follows that a δ -cover with $\delta = 2(\text{rch}_p \Lambda_p - \epsilon)$ is sufficient, and in some cases necessary, to guarantee that f_{nn} correctly classifies \mathcal{M}^ϵ .

Next we prove (2). As before let $q \in \mathcal{M}_i^\epsilon$. It is both necessary and sufficient for $q \in B(x, \text{rch}_p \Lambda_p)$ for some sample $x \in \mathcal{M}_i$ to guarantee that $f_{\mathcal{L}}(q) = i$, by definition of \mathcal{L} . The distance to the nearest sample x on \mathcal{M}_i is $d(q, x) \leq \epsilon + \delta$ for some $\delta > 0$. Thus it suffices that $\delta \leq \text{rch}_p \Lambda_p - \epsilon$. \square

In Appendix B we provide additional robustness results for nearest neighbors including: (1) a similar robustness guarantee as in Theorem 3 when noise is introduced into the samples and (2) that the decision boundary $\mathcal{D}_{f_{\text{nn}}}$ of f_{nn} approaches the decision axis as the sample density increases.

The bounds on δ in Theorem 3 are sufficient, but they are not always necessary. There exist manifolds where the bounds in Theorem 3 are pessimistic, and less dense samples corresponding to larger values of δ would suffice.

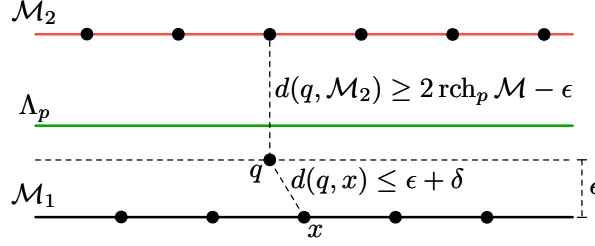


Figure 3: Proof of Theorem 3. The distance from a query point q to \mathcal{M}_2 , and thus the closest incorrectly labeled sample, is lower bounded by the distance necessary to reach the medial axis Λ_p plus the distance from Λ_p to \mathcal{M}_2 .

Next we will show a setting where bounds on δ similar to those in Theorem 3 are *necessary*. In this setting, the difference of a factor of 2 in δ between the sampling requirements of f_{nn} and $f_{\mathcal{L}}$ leads to an exponential gap between the sizes of X_{nn} and $X_{\mathcal{L}}$ necessary to achieve the same amount of robustness.

Define $\Pi_1 = \{x \in \mathbb{R}^d : \ell \leq x_1, \dots, x_k \leq \mu \text{ and } x_{k+1} = \dots = x_d = 0\}$; that is Π_1 is a subset of the $x_1 \dots x_k$ -plane bounded between the coordinates $[\ell, \mu]$. Similarly define $\Pi_2 = \{x \in \mathbb{R}^d : \ell \leq x_1, \dots, x_k \leq \mu \text{ and } x_{k+1} = \dots = x_{d-1} = 0 \text{ and } x_d = 2\}$. Note that Π_2 lies in the subspace $x_d = 2$; thus $\text{rch}_2 \Lambda_2 = 1$, where Λ_2 is the decision axis of $\Pi = \Pi_1 \cup \Pi_2$. In the $\|\cdot\|_2$ norm we can show that the gap in Theorem 3 is necessary for $\Pi = \Pi_1 \cup \Pi_2$. Furthermore the bounds we derive for δ -covers for Π for both f_{nn} and $f_{\mathcal{L}}$ are tight. Combined with well-known properties of covers, we get that the ratio $|X_{\mathcal{L}}|/|X_{\text{nn}}|$ is exponential in k .

Theorem 4. *Let $\Pi = \Pi_1 \cup \Pi_2$ as described above. Let $X_{\text{nn}}, X_{\mathcal{L}} \subset \Pi$ be minimum training sets necessary to guarantee that f_{nn} and $f_{\mathcal{L}}$ correctly classify \mathcal{M}^ϵ . Then we have that*

$$\frac{|X_{\mathcal{L}}|}{|X_{\text{nn}}|} \geq 2^{k/2} \quad (1)$$

Proof. Let $q \in \Pi_1^\epsilon$. Since Π_1 is flat, the distance to from q to the nearest sample $x \in \Pi_1$ is bounded as $\|q - x\|_2 \leq \sqrt{\epsilon^2 + \delta^2}$. For $f_{\text{nn}}(q) = 1$ we need that $\|q - x\|_2 \leq 2 - \epsilon$, and so it suffices that $\delta \leq 2\sqrt{1 - \epsilon}$. In this setting, this is also necessary; should δ be any larger a property placed sample on Π_2 can claim q in its Voronoi cell.

Similarly for $f_{\mathcal{L}}(q) = 1$ we need that $\|q - x\|_2 \leq 1$, and so it suffices that $\delta \leq \sqrt{1 - \epsilon^2}$. In this setting, this is also necessary; should δ be any larger, q lies outside of every $\|\cdot\|_2$ -ball $B(x, 1)$ and so \mathcal{L} is free to learn a decision boundary that misclassifies q .

Let $\mathcal{N}(\delta, \mathcal{M})$ denote the size of the minimum δ -cover of \mathcal{M} . Since Π is flat (has no curvature) and since the intersection of Π with a d -ball centered at a point on Π is a k -ball, a standard volume argument can be applied in the affine subspace $\text{aff } \Pi$ to conclude that $\mathcal{N}(\delta, \Pi) \in \Theta(\text{vol}_k \Pi / \delta^k)$. So we have

$$\begin{aligned} \frac{\mathcal{N}(\sqrt{1 - \epsilon^2}, \Pi)}{\mathcal{N}(2\sqrt{1 - \epsilon}, \Pi)} &= 2^k \left(\frac{1}{1 + \epsilon} \right)^{k/2} \\ &\geq 2^{k/2} \end{aligned}$$

Since Π is constant in both settings, the factor $\text{vol}_k \Pi$ as well as the constant factors hidden by $\Theta(\cdot)$ cancel. (Note that we are using the fact that Π_1, Π_2 have finite k -dimensional volume.) The inequality follows from the fact that the expression $(1 + \epsilon)^{-k/2}$ is monotonically decreasing on the interval $[0, 1]$ and takes value $2^{-k/2}$ at $\epsilon = 1$. \square

We have shown that both \mathcal{L} and nearest neighbor classifiers learn robust decision boundaries when provided sufficiently dense samples of \mathcal{M} . However there are settings where nearest neighbors is exponentially more sample-efficient than \mathcal{L} in achieving the same amount of robustness. We experimentally verify these theoretical results in Section 8.1.

6 X^ϵ is a Poor Model of \mathcal{M}^ϵ

Madry et al. (2018) suggest training a robust classifier with the help of an adversary which, at each iteration, produces ϵ -perturbations around the training set that are incorrectly classified. In our notation, this corresponds to learning a decision boundary that correctly classifies $X^\epsilon = \{x \in \mathbb{R}^d : \|x - X_i\|_2 \leq \epsilon \text{ for some training point } X_i\}$.

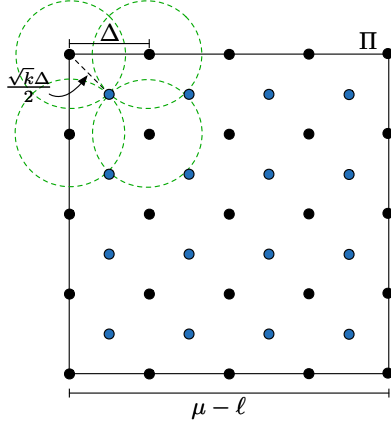


Figure 4: To construct an δ -cover we place sample points, shown here in black, along a regular grid with spacing Δ . The blue points are the furthest points of Π from the sample. To cover Π we need $\Delta = 2\delta/\sqrt{k}$.

We believe this approach is insufficiently robust in practice, as X^ϵ is often a poor model for \mathcal{M}^ϵ . In this section, we show that the volume $\text{vol } X^\epsilon$ is often a vanishingly small percentage of $\text{vol } \mathcal{M}^\epsilon$. These results shed light on why the ball-based learning algorithm \mathcal{L} defined in Section 5 is so much less sample-efficient than nearest neighbor classifiers. In Section 8.1 we experimentally verify these observations by showing that in high-dimensional space it is easy to find adversarial examples even after training against a strong adversary. For the remainder of this section we will consider the $\|\cdot\|_2$ norm.

Theorem 5. *Let $\mathcal{M} \subset \mathbb{R}^d$ be a k -dimensional manifold embedded in \mathbb{R}^d such that $\text{vol}_k \mathcal{M} < \infty$. Let $X \subset \mathcal{M}$ be a finite set of points sampled from \mathcal{M} . Suppose that $\epsilon \leq \text{rch}_2 \Xi$ where Ξ is the medial axis of \mathcal{M} , defined as in Dey (2007). Then the percentage of \mathcal{M}^ϵ covered by X^ϵ is upper bounded by*

$$\frac{\text{vol } X^\epsilon}{\text{vol } \mathcal{M}^\epsilon} \leq \frac{\pi^{k/2} \Gamma(\frac{d-k}{2} + 1)}{\Gamma(\frac{d}{2} + 1)} \frac{\epsilon^k}{\text{vol}_k \mathcal{M}} |X| \in \mathcal{O} \left(\left(\frac{2\pi}{d-k} \right)^{k/2} \frac{\epsilon^k}{\text{vol}_k \mathcal{M}} |X| \right). \quad (2)$$

As the codimension $(d-k) \rightarrow \infty$, Equation 2 approaches 0, for any fixed $|X|$.

Proof. Assuming the balls centered on the samples in X are disjoint we get the upper bound

$$\text{vol } X^\epsilon \leq \text{vol } B_\epsilon |X| = \frac{\pi^{d/2}}{\Gamma(\frac{d}{2} + 1)} \epsilon^d |X|. \quad (3)$$

This is identical to the reasoning in Equation 5.

The medial axis Ξ of \mathcal{M} is defined as the closure of the set of all points in \mathbb{R}^d that have two or more closest points on \mathcal{M} in the norm $\|\cdot\|_2$. The medial axis Ξ is similar to the decision axis Λ_2 , except that the nearest points do not need to be on distinct class manifolds. For $\epsilon \leq \text{rch}_2 \Xi$, we have the lower bound

$$\text{vol } \mathcal{M}^\epsilon \geq \text{vol}_{d-k} B_\epsilon^{d-k} \text{vol}_k \mathcal{M} = \frac{\pi^{(d-k)/2}}{\Gamma(\frac{d-k}{2} + 1)} \epsilon^{d-k} \text{vol}_k \mathcal{M}. \quad (4)$$

Combining Equations 3 and 4 gives the result. To get the asymptotic result we apply Stirling's approximation to get

$$\begin{aligned} \frac{\Gamma(\frac{d-k}{2} + 1)}{\Gamma(\frac{d}{2} + 1)} &\approx (2e)^{k/2} \frac{(d-k)^{(d-k+1)/2}}{d^{(d+1)/2}} \\ &= (2e)^{k/2} \frac{\left(\frac{d-k}{d}\right)^{(d+1)/2}}{(d-k)^{k/2}} \\ &= (2e)^{k/2} \frac{\left(1 - \frac{k}{d}\right)^{(d+1)/2}}{(d-k)^{k/2}} \\ &\approx \left(\frac{2}{d-k}\right)^{k/2}. \end{aligned}$$

The last step follows from the fact that $\lim_{d \rightarrow \infty} (1 - k/d)^{(d+1)/2} = e^{-k/2}$, where e is the base of the natural logarithm. \square

In high codimension, even moderate under-sampling of \mathcal{M} leads to a significant loss of coverage of \mathcal{M}^ϵ because the volume of the union of balls centered at the samples shrinks faster than the volume of \mathcal{M}^ϵ . Theorem 5 states that in high codimensions the fraction of \mathcal{M}^ϵ covered by X^ϵ goes to 0. Almost nothing is covered by X^ϵ for training set sizes that are realistic in practice. Thus X^ϵ is a poor model of \mathcal{M}^ϵ , and high classification accuracy on X^ϵ does not imply high accuracy in \mathcal{M}^ϵ .

Note that an alternative way of defining the ratio $\text{vol } X^\epsilon / \text{vol } \mathcal{M}^\epsilon$ is as $\text{vol}(X^\epsilon \cap \mathcal{M}^\epsilon) / \text{vol } \mathcal{M}^\epsilon$. This is equivalent in our setting since $X \subset \mathcal{M}$ and so $X^\epsilon \subset \mathcal{M}^\epsilon$.

For the remainder of the section we provide intuition for Theorem 5 by considering the special case of k -dimensional planes. Define $\Pi = \{x \in \mathbb{R}^d : \ell \leq x_1, \dots, x_k \leq \mu \text{ and } x_{k+1} = \dots = x_d = 0\}$; that is Π is a subset of the $x_1 \dots x_k$ -plane bounded between the coordinates $[\ell, \mu]$. Recall that a δ -cover of a manifold \mathcal{M} in the norm $\|\cdot\|_2$ is a finite set of points X such that for every $x \in \mathcal{M}$ there exists X_i such that $\|x - X_i\|_2 \leq \delta$. It is easy to construct an *explicit* δ -cover X of Π : place sample points at the vertices of a regular grid, shown in Figure 4 by the black vertices. The centers of the cubes of this regular grid, shown in blue in Figure 4, are the furthest points from the samples. The distance from the vertices of the grid to the centers is $\sqrt{k}\Delta/2$ where Δ is the spacing between points along an axis of the grid. To construct a δ -cover we need $\sqrt{k}\Delta/2 = \delta$ which gives a spacing of $\Delta = 2\delta/\sqrt{k}$. The size of this sample is $|X| = \left(\frac{\sqrt{k}(\mu-\ell)}{2\delta}\right)^k$. Note that $|X|$ scales exponentially in k , the dimension of Π , not in d , the dimension of the embedding space.

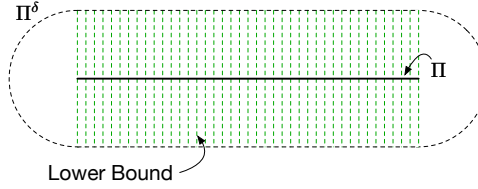


Figure 5: An illustration of the lower bound technique used in Equation 6. The volume $\text{vol } \Pi^\delta$ shown in the black dashed lines, is bounded from below by placing a $(d-k)$ -dimensional ball of radius δ at each point of Π , shown in green. In this illustration, a 1-dimensional manifold is embedded in 2 dimensions, so these balls are 1-dimensional line segments.

Recall that Π^δ is the δ -tubular neighborhood of Π . The δ -balls around X , which comprise X^δ , cover Π and so any robust approach that guarantees correct classification within X^δ will achieve perfect accuracy on Π . However, we will show that X^δ covers only a vanishingly small fraction of Π^δ . Let B_δ denote the d -ball of radius δ centered at the origin. An upper bound on the volume of X^δ is

$$\text{vol } X^\delta \leq \text{vol } B_\delta |X| = \frac{\pi^{d/2}}{\Gamma(\frac{d}{2} + 1)} \delta^d \left(\frac{\sqrt{k}(\mu-\ell)}{2\delta}\right)^k = \frac{\pi^{d/2}}{\Gamma(\frac{d}{2} + 1)} \delta^{(d-k)} \left(\frac{\sqrt{k}(\mu-\ell)}{2}\right)^k. \quad (5)$$

Next we bound the volume $\text{vol } \Pi^\delta$ from below. Intuitively, a lower bound on the volume can be derived by placing a $(d-k)$ -dimensional ball in the normal space at each point of Π and integrating the volumes. Figure 4 (Right) illustrates the lower bound argument in the case of $k=1, d=2$.

$$\text{vol } \Pi^\delta \geq \text{vol}_{d-k} B_\delta^{d-k} \text{vol}_k \Pi = \frac{\pi^{(d-k)/2}}{\Gamma(\frac{d-k}{2} + 1)} \delta^{d-k} (\mu-\ell)^k. \quad (6)$$

Combining Equations 5 and 6 gives an upper bound on the percentage of Π^δ that is covered by X^ϵ .

$$\frac{\text{vol } X^\delta}{\text{vol } \Pi^\delta} \leq \frac{\pi^{k/2} \Gamma(\frac{d-k}{2} + 1)}{\Gamma(\frac{d}{2} + 1)} \left(\frac{\sqrt{k}}{2}\right)^k. \quad (7)$$

Notice that the factors involving δ and $(\mu-\ell)$ cancel. Figure 6 (Left) shows that this expression approaches 0 as the codimension $(d-k)$ of Π increases.

Suppose we set $\delta=1$ and construct a 1-cover of Π . The number of points necessary to cover Π with balls of radius 1 depends *only* on k , not the embedding dimension d . However the number of points necessary to cover the tubular neighborhood Π^1 with balls of radius 1 increases depends on *both* k and d . In Theorem 6 we derive a lower bound on the number of samples necessary to cover Π^1 .

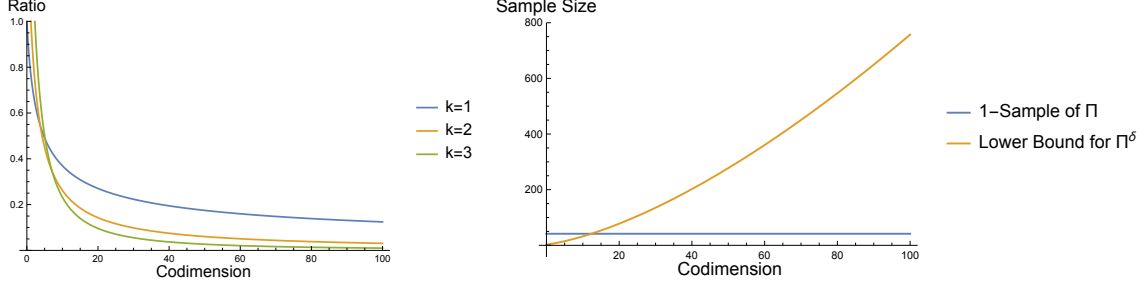


Figure 6: We plot the upper bound in Equation 7 on the left. As the codimension increases, the percentage of volume of Π^1 covered by 1-balls around the 1-sample approaches 0. On the right we plot the number of samples necessary to cover Π , shown in blue, against the number of samples necessary to cover Π^1 , shown in orange, as the codimension increases.

Theorem 6. Let Π be a bounded k -flat as described above, bounded along each axis by $\ell < \mu$. Let n denote the number of samples necessary to cover the 1-tubular neighborhood Π^1 of Π with $\|\cdot\|_2$ -balls of radius 1. That is let n be the minimum value for which there exists a finite sample X of size n such that $\Pi^1 \subset \cup_{x \in X} B(x, 1) = X^1$. Then

$$n \geq \frac{\pi^{-k/2} \Gamma(\frac{d}{2} + 1)}{\Gamma(\frac{d-k}{2} + 1)} (\mu - \ell)^k \in \Omega\left(\left(\frac{d-k}{2\pi}\right)^{k/2} (\mu - \ell)^k\right). \quad (8)$$

Proof. We first construct an upper bound by generously assuming that the balls centered at the samples are disjoint. That is

$$\frac{\text{vol } X^\delta}{\text{vol } \Pi^\delta} \leq \frac{n \text{ vol } B_\delta}{\text{vol } \Pi^\delta}. \quad (9)$$

To guarantee that $\Pi^1 \subset \cup_{x \in X} B(x, 1) = X^1$ we set the left hand side of Equation 9 equal to 1 and solve for n .

$$\begin{aligned} 1 &= \frac{\text{vol } X^\delta}{\text{vol } \Pi^\delta} \leq \frac{n \text{ vol } B_\delta}{\text{vol } \Pi^\delta} \\ n &\geq \frac{\text{vol } \Pi^\delta}{\text{vol } B_\delta} \\ &\geq \frac{\pi^{-k/2} \Gamma(\frac{d}{2} + 1)}{\Gamma(\frac{d-k}{2} + 1)} \left(\frac{\mu - \ell}{\delta}\right)^k \end{aligned}$$

The last inequality follows from Equation 6. Setting $\delta = 1$ gives the result. The asymptotic result is similar to the argument in the proof of Theorem 5. \square

Theorem 6 states that, in general, it takes many fewer samples to accurately model \mathcal{M} than to model \mathcal{M}^ϵ . Figure 6 (Right) compares the number of points necessary to construct a 1-cover of Π with the lower bound on the number necessary to cover Π^1 from Theorem 6. The number of points necessary to cover Π^1 increases as $\Omega((d-k)^{k/2})$, scaling polynomially in d and exponentially in k . In contrast, the number necessary to construct a 1-cover of Π remains constant as d increases, depending only on k .

Our lower bound of $\Omega((d-k)^{k/2})$ samples is similar to the work of Schmidt et al. (2018) who prove that, in the simple Gaussian setting, robustness *requires* as much as $\Omega(\sqrt{d})$ more samples. Their arguments are statistical while ours are geometric.

Approaches that produce robust classifiers by generating adversarial examples in the ϵ -balls centered on the training set do not accurately model \mathcal{M}^ϵ , and it will take *many* more samples to do so. If the method behaves arbitrarily outside of the ϵ -balls that define X^ϵ , adversarial examples will still exist and it will likely be easy to find them. The reason deep learning has performed so well on a variety of tasks, in spite of the brittleness made apparent by adversarial examples, is because it is much easier to perform well on \mathcal{M} than it is to perform well on \mathcal{M}^ϵ .

7 A Lower Bound on Model Expressiveness

7.1 A Simple Example

Consider the case of two concentric circles C_1, C_2 with radii $r_1 < r_2$ respectively, as illustrated in Figure 7. Each circle represents a different class of data. Suppose that we train a parametric model $f(x; \theta)$ with p parameters so that for $x \in C_1$, $f(x; \theta) > 0$ and for $x \in C_2$, $f(x; \theta) < 0$. How does the number of parameters p necessary to ensure that such a decision boundary can be expressed by $f(\cdot; \theta)$ increase as the gap between C_1 and C_2 decreases?

Suppose that we first lift C_1 and C_2 to a parabola in \mathbb{R}^3 via map $\phi(x_1, x_2) = (x_1, x_2, x_1^2 + x_2^2)$. That is, we construct the sets $C_1^+ = \{\phi(x_1, x_2) : (x_1, x_2) \in C_1\}$ and similarly for C_2^+ . After applying ϕ , C_1^+ and C_2^+ are *linearly separable* for any $r_2 - r_1 > 0$. The linear decision boundary in \mathbb{R}^3 maps back to a circle in \mathbb{R}^2 that separates C_1 and C_2 . This is not the case for deep networks; the number of parameters necessary to separate C_1 and C_2 will depend on the gap $r_2 - r_1$.

In the important special case where f is parameterized by a fully connected deep network with ℓ layers, h hidden units per layer, and ReLU activations, Raghu et al. (2017) prove that f subdivides the input space into convex polytopes. In each convex polytope, f defines a linear function that agrees on the boundary of the polytope with its neighbors. They showed that, when the inputs are in \mathbb{R}^2 , the number of polytopes in the subdivision is at most $\mathcal{O}(h^{2\ell})$ (Raghu et al. (2017)[Theorem 1]).

Let \mathcal{S}_f denote the subdivision of space into convex polytopes induced by f . Consider the decision boundary $\mathcal{D}_f = \{x \in \mathbb{R}^d : f(x; \theta) = 0\}$ of f . \mathcal{D}_f can be constructed by examining each polytope $P \in \mathcal{S}_f$ and solving the linear equation $f_P(x) = 0$ where f_P is the linear function defined on P by f . Since f_P is linear the solution is either (1) the empty set, (2) a *single* line segment, or (3) all of P . Case (3) is a degenerate case and there are ways to perturb f by an infinitesimally small amount such that case (3) never occurs and the classification accuracy is unchanged. Thus we conclude that \mathcal{D}_f is a piecewise-linear curve comprised of line segments. (In higher dimensions \mathcal{D}_f is composed of subsets of hyperplanes.) See Figure 7.

Suppose that \mathcal{D}_f separates C_1 from C_2 and let $s \in \mathcal{D}_f$ be a line segment of the decision boundary. Since s lies in the space between C_1 and C_2 , the length $|s| \leq 2\sqrt{r_2^2 - r_1^2}$, which is tight when s is tangent to C_1 and touches C_2 at both of its endpoints. For \mathcal{D}_f to separate C_1 from C_2 , \mathcal{D}_f must make a full rotation of 2π around the origin. The portion of this rotation that s can contribute is upper bounded by $2 \arccos \frac{r_1}{r_2}$. Thus the number of line segments that comprise \mathcal{D}_f is lower bounded by $\frac{\pi}{\arccos \frac{r_1}{r_2}}$.

As $r_2 \rightarrow r_1$, the minimum number of segment necessary to separate C_1 from C_2 $\frac{\pi}{\arccos \frac{r_1}{r_2}} \rightarrow \infty$. Since each polytope $P \in \mathcal{S}_f$ can contribute at most one line segment to \mathcal{D}_f , the size of the model necessary to represent a decision boundary that separates C_1 from C_2 also increases as the circles get closer together.

Now consider C_1^ϵ and C_2^ϵ under the $\|\cdot\|_2$ norm, defined as $C_i^\epsilon = \{x \in \mathbb{R}^2 : \|x - C_i\|_2 \leq \epsilon\}$. Suppose that a fully connected network f described as above has sufficiently many parameters to represent a decision boundary that separates C_1 from C_2 . Is f also capable of learning a *robust* decision boundary that separates C_1^ϵ from C_2^ϵ ?

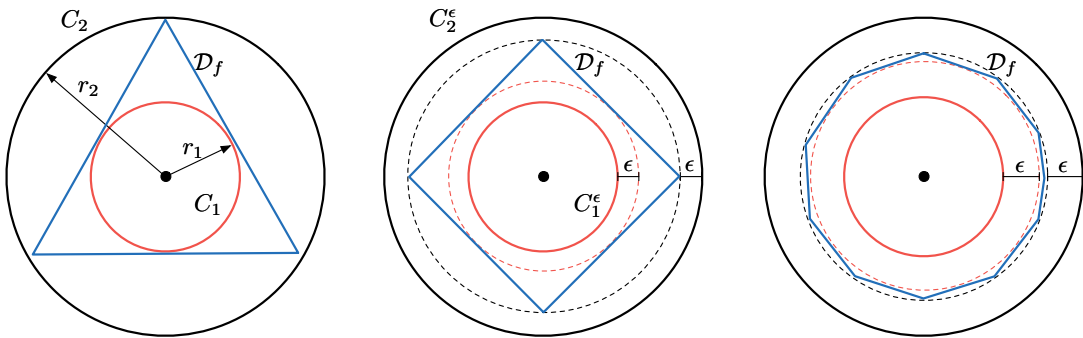


Figure 7: Separating two classes of data sampled from C_1 and C_2 may require a decision boundary \mathcal{D}_f with only a few linear segments. However a decision boundary \mathcal{D}_f that is robust to ϵ -perturbations must lie in gap between C_1^ϵ and C_2^ϵ . Learning a robust decision boundary may require more linear segments and thus a more expressive model. As we increase ϵ , demanding a more robust decision boundary, the gap between C_1^ϵ and C_2^ϵ decreases, and so the number of linear segments increases towards ∞ .

For \mathcal{D}_f to separate C_1^ϵ from C_2^ϵ it must lie in the region between C_1^ϵ and C_2^ϵ . In this setting each segment can contribute at most $2 \arccos \frac{r_1 + \epsilon}{r_2 - \epsilon}$ to the full 2π rotation around the origin. The minimum number of line segments

that comprise a robust decision boundary \mathcal{D}_f is lower bounded by $\frac{\pi}{\arccos \frac{r_1 + \epsilon}{r_2 - \epsilon}}$. As $\epsilon \rightarrow \frac{r_2 - r_1}{2}$ this quantity approaches ∞ . Even if f is capable of separating C_1 from C_2 we can choose ϵ such that $\frac{\pi}{\arccos \frac{r_1 + \epsilon}{r_2 - \epsilon}} \in \omega(h^{2\ell})$.

This simple example shows that learning decision boundaries that are robust to ϵ -adversarial examples may require substantially more powerful models than what is required to learn the original distributions. Furthermore the amount of additional resources necessary is dependent upon the amount of robustness required.

7.2 An Exponential Lower Bound

We present an exponential lower bound on the number of linear regions necessary to represent a decision boundary that is robust to $\|\cdot\|_2$ -perturbations of at most $\epsilon \leq \text{rch}_2 \Lambda_2 - \tau$, in the simple case of two concentric $(d-1)$ -spheres.

Theorem 7. *Let $S_1, S_2 \subset \mathbb{R}^d$ be two concentric $(d-1)$ -spheres with radii $r_1 < r_2$ respectively and let $S = S_1 \cup S_2$. Let $f : \mathbb{R}^d \rightarrow \mathbb{R}$ be a fully connected neural network with ReLU activations. Suppose that f correctly classifies $S^{\text{rch}_2 \Lambda_2 - \tau}$ for some $\tau \in [0, \text{rch}_2 \Lambda_2]$. Said differently, the decision boundary of f lies in a τ -tubular neighborhood of the decision axis, $\mathcal{D}_f \subset \Lambda_2^\tau$. Then the number of linear regions N into which f subdivides \mathbb{R}^d is lower bounded as*

$$N \geq 2\sqrt{\pi} \frac{\Gamma(\frac{d+1}{2})}{\Gamma(\frac{d}{2})} \left(\frac{r_1 + \text{rch}_2 \Lambda_2}{4\tau} \right)^{\frac{d-1}{2}}. \quad (10)$$

Written asymptotically, $N \in \Omega \left(\frac{\sqrt{d}}{2^{\frac{d}{2}}} \left(\frac{r_1 + \text{rch}_2 \Lambda_2}{\tau} \right)^{\frac{d-1}{2}} \right)$

Proof. For f to be robust to ϵ -adversarial examples for $\epsilon \leq \text{rch}_2 \Lambda_2 - \tau$ the decision boundary $\mathcal{D}_f \subset \Lambda^\tau$. The boundary of Λ^τ is comprised of two disjoint $(d-1)$ -spheres, which we will denote as $\partial\Lambda_1^\tau$ and $\partial\Lambda_2^\tau$ with radii $r_1 + \text{rch}_2 \Lambda_2 - \tau$ and $r_1 + \text{rch}_2 \Lambda_2 + \tau$ respectively. (It is standard in topology to use the ∂ symbol to denote the boundary of a topological space.)

The isoperimetric inequality states that a $(d-1)$ -sphere minimizes the $(d-1)$ -dimensional volume (thought of as “surface area”) across all sets with fixed d -dimensional volume (thought of as “volume”). Since $\mathcal{D}_f \subset \Lambda^\tau$, the d -dimensional volume enclosed by \mathcal{D}_f is at least as large as that of $\partial\Lambda_1^\tau$ and so we have that $\text{surf } \partial\Lambda_1^\tau \leq \text{surf } \mathcal{D}_f$.

Now consider any $(d-1)$ -dimensional linear facet Π of the decision boundary \mathcal{D}_f . The normal space of Π is 1-dimensional; let \mathbf{n} denote a unit vector orthogonal to Π . (There are two possible choices \mathbf{n} and $-\mathbf{n}$.) Due to the spherical symmetry of Λ^τ and the fact that $\Pi \subset \Lambda^\tau$, the diameter of Π is maximized when Π is tangent to $\partial\Lambda_1^\tau$ at $(r_1 + \text{rch}_2 \Lambda_2 - \tau)\mathbf{n}$ (or $-(r_1 + \text{rch}_2 \Lambda_2 - \tau)\mathbf{n}$) and intersects $\partial\Lambda_2^\tau$. In pursuit of an upper bound, we will assume without loss of generality that Π has these properties. Let o denote the origin, $x = (r_1 + \text{rch}_2 \Lambda_2 - \tau)\mathbf{n}$, and $y \in \Pi \cap \partial\Lambda_2^\tau$. We consider the right triangle $\triangle oxy$ with right angle at x . By basic properties of right triangles, $\frac{\text{diam } \Pi}{2} \leq \|x - y\|_2 = \sqrt{(r_1 + \text{rch}_2 \Lambda_2 + \tau)^2 - (r_1 + \text{rch}_2 \Lambda_2 - \tau)^2} = \sqrt{4\tau(r_1 + \text{rch}_2 \Lambda_2)}$. It follows that Π is contained in a $(d-1)$ -dimensional ball of radius $\sqrt{4\tau(r_1 + \text{rch}_2 \Lambda_2)}$. In particular the $(d-1)$ -dimensional volume of Π is bounded as $\text{vol}_{d-1}(\Pi) \leq \text{vol}_{d-1} B(0, \sqrt{4\tau(r_1 + \text{rch}_2 \Lambda_2)})$. The $(d-1)$ -dimensional volume of \mathcal{D}_f (again thought of as “surface area”), is equal to the sum of the $(d-1)$ -dimensional volumes of the linear facets that comprise \mathcal{D}_f . Combining these inequalities gives the result.

$$\begin{aligned} \frac{2\pi^{\frac{d}{2}}}{\Gamma(\frac{d}{2})} (r_1 + \text{rch}_2 \Lambda_2)^{d-1} &= \text{surf } \partial\Lambda_1^\tau \leq \text{surf } \mathcal{D}_f \\ &\leq N \text{vol}_{d-1} B(0, \sqrt{4\tau(r_1 + \text{rch}_2 \Lambda_2)}) \\ &\leq N \frac{\pi^{\frac{d-1}{2}}}{\Gamma(\frac{d+1}{2})} (4\tau(r_1 + \text{rch}_2 \Lambda_2))^{\frac{d-1}{2}} \\ 2\sqrt{\pi} \frac{\Gamma(\frac{d+1}{2})}{\Gamma(\frac{d}{2})} \left(\frac{r_1 + \text{rch}_2 \Lambda_2}{4\tau} \right)^{\frac{d-1}{2}} &\leq N \end{aligned}$$

□

Prior work has experimentally verified that increasing the size of deep networks improves robustness (Madry et al. (2018)). Theorem 7 proves that there are settings in which robustness *requires* larger models.

8 Experiments

8.1 High Codimension Reduces Robustness

Section 6 suggests that as the codimension increases it should become easier to find adversarial examples. To verify this, we introduce two synthetic datasets, CIRCLES and PLANES, which allow us to carefully vary the codimension while maintaining dense samples. The CIRCLES dataset consists of two concentric circles in the x_1 - x_2 -plane, the first with radius $r_1 = 1$ and the second with radius $r_2 = 3$, so that $\text{rch}_2 \Lambda_2 = 1$. We densely sample 1000 random points on each circle for both the training and the test sets. The PLANES dataset consists of two 2-dimensional planes, the first in the $x_d = 0$ and the second in $x_d = 2$, so that $\text{rch}_2 \Lambda_2 = 1$. The first two axis of both planes are bounded as $-10 \leq x_1, x_2 \leq 10$, while $x_3 = \dots = x_{d-1} = 0$. We sample the training set at the vertices of the grid described in Section 6, and the test set at the centers of the grid cubes, the blue points in Figure 4. Both planes are sampled so that the 1-tubular neighborhood X^1 covers the underlying planes, where X is the training set. See Figure 8 for a visualization of CIRCLES and PLANES.

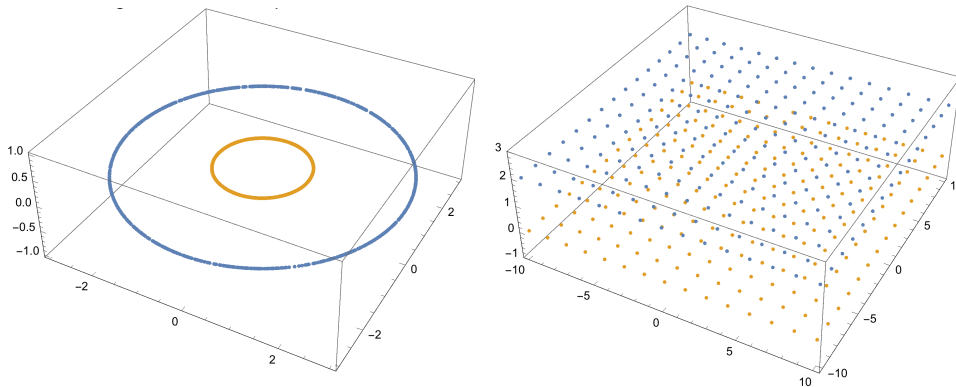


Figure 8: We create two synthetic datasets which allow us to perform controlled experiments on the affect of codimension on adversarial examples. **Left:** CIRCLES, **Right:** PLANES

We consider two attacks, the fast gradient sign method (FGSM) (Goodfellow et al. (2014)) and the basic iterative method (BIM) (Kurakin et al. (2016)) under $\|\cdot\|_2$. We use the implementations provided in the cleverhans library (Papernot et al. (2018)). Further implementation details are provided in Appendix E. Our experimental results are averaged over 20 retrainings of our model architecture, using Adam (Kingma and Ba (2015)). Further implementation details are provided in Appendix E.

Figure 9 (Top Left, Bottom Left) shows the robustness of naturally trained networks to FGSM and BIM attacks on the CIRCLES dataset as we increase the codimension. For both attacks we see a steady decrease in robustness as we increase the codimension, on average. The result is reproducible with other optimization procedures; Figure 15 in Appendix C.1 shows the results for SGD.

In Figure 9 (Top Right, Bottom Right), we use a nearest neighbor (NN) classifier to classify the adversarial examples generated by FGSM and BIM for our naturally trained networks on CIRCLES. Nearest neighbors is robust even when the codimension is high, as long as the low-dimensional data manifold is well sampled. This is a consequence of the fact that the Voronoi cells of the samples are elongated in the directions normal to the data manifold when the sample is dense (Dey (2007)).

Madry et al. (2018) propose training against a projected gradient descent (PGD) adversary to improve robustness. Section 6 suggests that this should be insufficient to guarantee robustness, as X^ϵ is often a poor model for \mathcal{M}^ϵ . We follow the adversarial training procedure of Madry et al. (2018) by against a PGD adversary with $\epsilon = 1$ under $\|\cdot\|_2$ -perturbations on the PLANES dataset. Figure 10 (Left) shows that it is still easy to find adversarial examples for $\epsilon < 1$ and that as the codimension increases we can find adversarial examples for decreasing values of ϵ . In contrast, a nearest neighbor classifier (Right) achieves perfect robustness for all ϵ on this data.

The PLANES dataset is sampled so that the training set is a 1-cover of the underlying planes, which requires 450 sample points. Figure 11 shows the results of increasing the sampling density to a 0.5-cover (1682 samples) and a 0.25-cover (6498 samples). Increasing the sampling density improves the robustness of adversarial training at the same codimension and particularly in low-codimension. However adversarial training with a substantially larger training set does not produce a classifier as robust as a nearest neighbor classifier on a much smaller training set. Nearest neighbors is much more sample efficient than adversarial training, as predicted by Theorem 3.

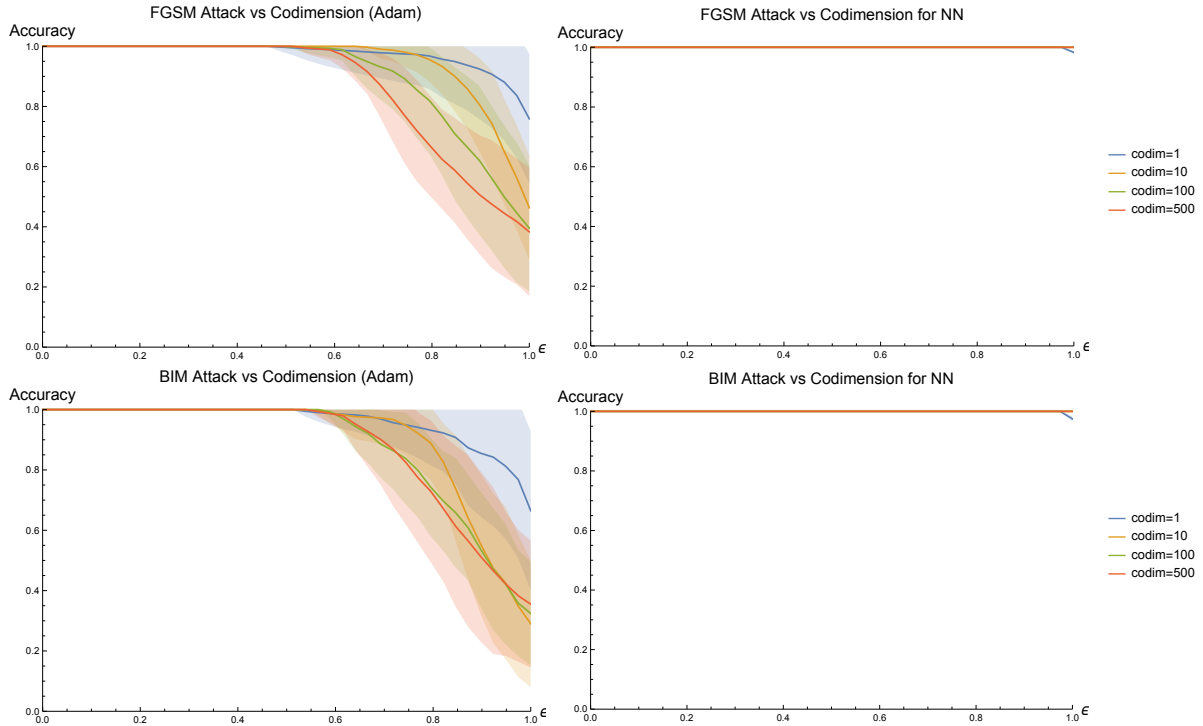


Figure 9: As the codimension increases the robustness of decision boundaries learned by Adam on naturally trained networks decreases steadily. **Top Left:** Effectiveness of FGSM attacks as codimension increases. **Bottom Left:** BIM attacks. **Top and Bottom Right:** A nearest neighbor classifier exhibits essentially perfect accuracy to the adversarial examples generated for our naturally trained networks by FGSM and BIM for all ϵ and codimension.

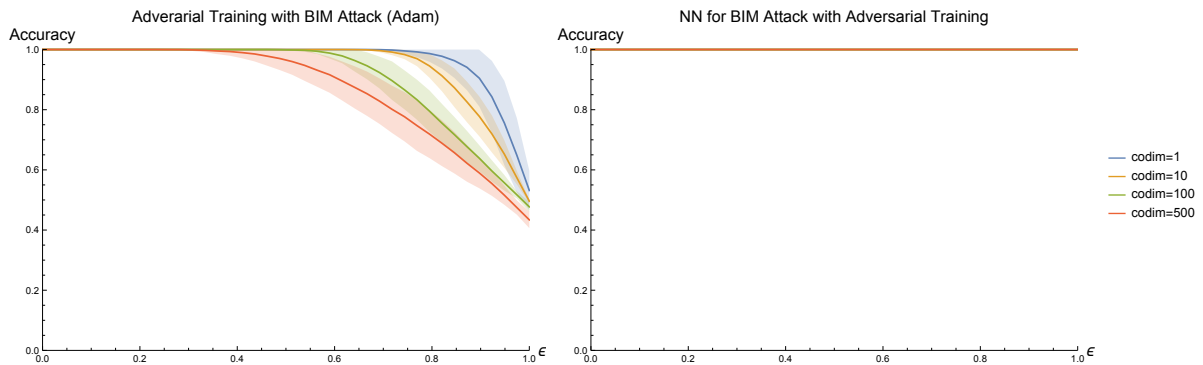


Figure 10: **Left:** Training using the adversarial training procedure of Madry et al. (2018) is no guarantee of robustness; as the codimension increases it becomes easier to find adversarial examples using BIM attacks. **Right:** The performance of a nearest neighbor classifier on this data is perfect for all ϵ and codimension.

8.2 Adversarial Perturbations are in the Directions Normal to the Data Manifold

Let η_x be an adversarial perturbation generated by FGSM with $\epsilon = 1$ at $x \in \mathcal{M}$. Note that the adversarial example is constructed as $\hat{x} = x + \eta_x$. In Figure 12 we plot a histogram of the angles $\angle(\eta_x, N_x\mathcal{M})$ between η_x and the normal space $N_x\mathcal{M}$ for the CIRCLES dataset in codimensions 1, 10, 100, and 500. In codimension 1, 88% of adversarial perturbations make an angle of less than 10° with the normal space. Similarly in codimension 10, 97%, in codimension 100, 96%, and in codimension 500, 93%. As Figure 12 shows, nearly all adversarial perturbations make an angle less than 20° with the normal space. Our results are averaged over 20 retrainings of the model using SGD.

Throughout this paper we’ve argued that high codimension is a key source of the pervasiveness of adversarial

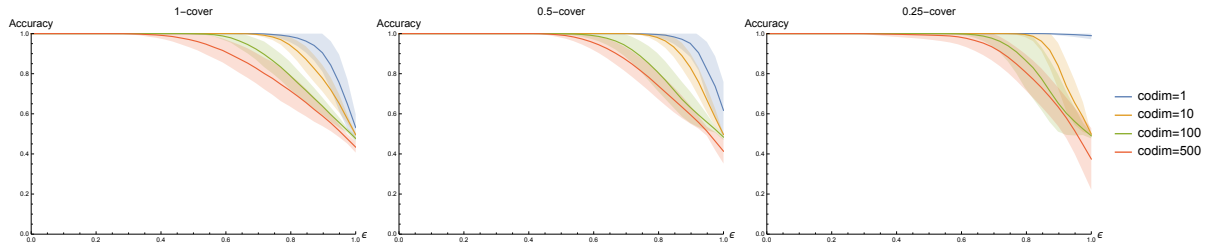


Figure 11: Adversarial training of Madry et al. (2018) on the PLANES dataset with a 1-cover (left), consisting of 450 samples, a 0.5-cover (center), 1682 samples, and a 0.25-cover (right), 6498 samples. Increasing the sampling density improves robustness at the same codimension. However even training on a significantly denser training set does not produce a classifier as robust as a nearest neighbor classifier on a much sparser training set, Figure 10 (Right).

examples. Figure 12 shows that, when the underlying data manifold is well sampled, adversarial perturbations are well aligned with the normal space. When the codimension is high, there are many directions normal to the manifold and thus many directions in which to construct adversarial perturbations.

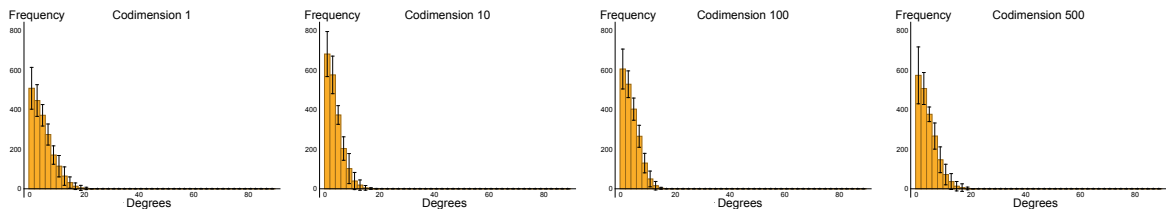


Figure 12: Histograms of the angle deviations of FGSM perturbations from the normal space for the CIRCLES dataset in, from right to left, codimensions 1, 10, 100, and 500. Nearly all perturbations make an angle of less than 20° with the normal space.

8.3 A Gradient-Free Geometric Attack

Most current attacks rely on the gradient of the loss function at a test sample to find a direction towards the decision boundary. Partial resistance against such attacks can be achieved by obfuscating the gradients, but Athalye et al. (2018) showed how to circumvent such defenses. Brendel et al. (2018) propose a gradient-free attack for $\|\cdot\|_2$, that starts from a misclassified point and walks toward the original point.

In this section we propose a gradient-free attack that only requires oracle access to a model, meaning we only query the model for a prediction. Consider a point $x \in X_{\text{test}}$ and the $\|\cdot\|_p$ -ball $B(x, r)$ centered at x of radius r . To construct an adversarial perturbation $\eta_x \in B(0, r)$, giving an adversarial example $\hat{x} = x + \eta_x$, we project every point in X_{test} onto $B(x, r)$ and query the oracle for a prediction for each point. If there exists $y \in X_{\text{test}}$ that is projected to a point $y' \in B(x, r)$ and that is classified differently from x , we take $\eta_x = y' - x$, otherwise $\eta_x = 0$. This incredibly simple attack reduces the accuracy of the pretrained robust model of Madry et al. (2018) for $\|\cdot\|_\infty$ and $\epsilon = 0.3$ to 90.6%, less than two percent shy of the current SOTA for whitebox attacks, 88.79% (Zheng et al. (2018)).

Simple datasets, such as CIRCLES and PLANES, allow us to diagnose issues in learning algorithms in settings where we understand how the algorithm should behave. For example Athalye et al. (2018) state that the work of Madry et al. (2018) does not suffer from obfuscated gradients. In Appendix D we provide evidence that Madry et al. (2018) *does* suffer from the obfuscated gradients problem, failing one of Athalye et al. (2018)'s criteria for detecting obfuscated gradients.

8.4 MNIST

To explore performance on a more realistic dataset, we compared nearest neighbors with robust and natural models on MNIST. We considered two attacks: BIM under l_∞ norm against the natural and robust models as well as a

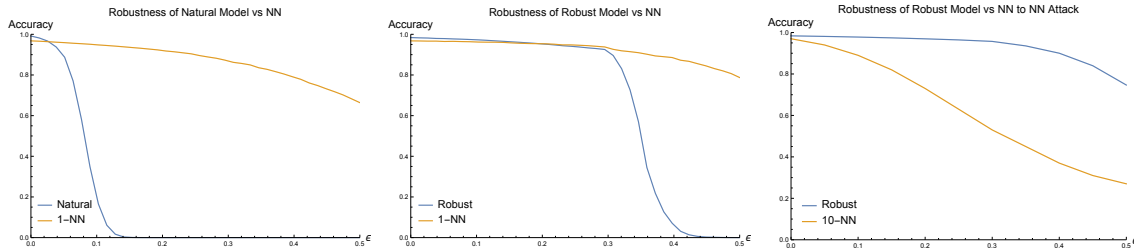


Figure 13: Robustness of nearest neighbors on MNIST. **Left:** Performance on l_∞ BIM attack against a naturally trained model. **Center:** The same for the adversarially trained convolutional models of Madry et al. (2018). **Right:** Performance of the robust model and nearest neighbors on examples generated by a custom attack on nearest neighbors.

custom attack against nearest neighbors. Each of these attacks are generated from the MNIST test set. Architecture details can be found in Appendix E. Figure 13 (Left) shows that nearest neighbors is substantially more robust to BIM attacks than the naturally trained model. Figure 13 (Center) shows that nearest neighbors is comparable to the robust model up to $\epsilon = 0.3$, which is the value for which the robust model was trained. After $\epsilon = 0.3$, nearest neighbors is substantially more robust to BIM attacks than the robust model. At $\epsilon = 0.5$, nearest neighbors maintains accuracy of 78% to adversarial perturbations that cause the accuracy of the robust model to drop to 0%. In Appendix C.2 we provide a similar result for FGSM attacks.

Figure 13 (Right) shows the performance of nearest neighbors and the robust model on adversarial examples generated for nearest neighbors. The nearest neighbor attacks are generated as follows: iteratively find the k nearest neighbors and compute an attack direction by walking away from the neighbors in the true class and toward the neighbors in other classes. We find that nearest neighbors is able to be tricked by this approach, but the robust model is not. This indicates that the errors of these models are distinct and suggests that ensemble methods may be effective.

A closer investigation shows strong qualitative differences between the BIM adversarial examples and the examples generated for nearest neighbors. The top row of Figure 14 shows four samples from the MNIST test set. The second and third rows show adversarial examples generated from those four samples for nearest neighbors and the robust model respectively. We observe an immediate qualitative difference between rows two and three: the adversarial examples for the nearest neighbors classifier begin to look like numbers from the target class! It can reasonably be argued that the fact that the classifications of the robust model do not change is as much of an error as being fooled by a standard adversarial example. For example the rightmost image of row two in Figure 14 would be classified as an 8 by most people, while the robust model is confident this image is a 0 with confidence 0.91. The confidence value of the robust model should decrease significantly for this image. This provides evidence that nearest neighbors is doing a better job of the learning the *human* decision boundary between numbers.

9 Conclusion

We have presented a geometric framework for proving robustness guarantees for learning algorithms. Our framework is general and can be used to describe the robustness of any classifier. We have shown that no single model can be simultaneously robust to attacks under all norms, that nearest neighbor classifiers are theoretically more sample efficient than adversarial training, and that robustness requires larger deep ReLU networks. Most importantly, we have highlighted the role of codimension in contributing to adversarial examples and verified our theoretical contributions with experimental results.

We believe that a geometric understanding of the decision boundaries learned by deep networks will lead to both new geometrically inspired attacks and defenses. In Section 8.3 we provided a novel gradient-free geometric attack in support of this claim. Finally we believe future work into the geometric properties of decision boundaries learned by various optimization procedures will provide new techniques for black-box attacks.

Acknowledgments We thank Horia Mania, Ozan Sener, Sohil Shah, Jonathan Shewchuk, and Tess Smidt for providing valuable comments on an earlier draft of this work. Additionally we thank Tess Smidt for providing the compute resources for this work.

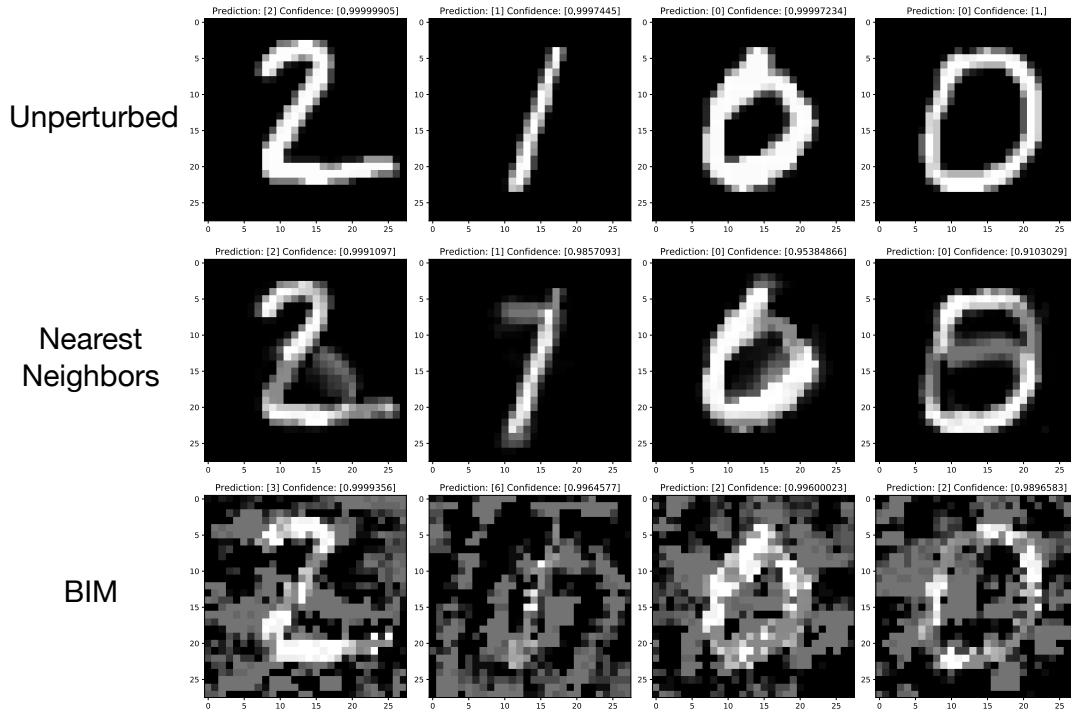


Figure 14: Comparison of adversarial examples for nearest neighbor with adversarial examples for Madry et al. (2018). The top row is the original data that the examples were generated from. Each figure is labelled with the predictions from robust neural network. An immediate qualitative difference between adversarial examples for nearest neighbors and those for the robust model is apparent; the nearest neighbor examples are starting to look like numbers from a target class.

References

- N. Amenta and M. W. Bern. Surface reconstruction by voronoi filtering. *Discrete & Computational Geometry*, 1999.
- N. Amenta, M. W. Bern, and D. Eppstein. The crust and the beta-skeleton: Combinatorial curve reconstruction. *Graphical Models and Image Processing*, 1998.
- N. Amenta, S. Choi, T. K. Dey, and N. Leekha. A simple algorithm for homeomorphic surface reconstruction. *International Journal of Computational Geometry and Applications*, 2002.
- A. Athalye, N. Carlini, and D. A. Wagner. Obfuscated gradients give a false sense of security: Circumventing defenses to adversarial examples. In *ICML*, 2018.
- H. Blum. A transformation for extracting new descriptors of shape. *Models for Perception of Speech and Visual Forms*, 1967.
- J. Boissonnat and A. Ghosh. Manifold reconstruction using tangential delaunay complexes. *Discrete & Computational Geometry*, 51, 2014.
- W. Brendel, J. Rauber, and M. Bethge. Decision-based adversarial attacks: Reliable attacks against black-box machine learning models. In *ICLR*, 2018.
- S. Cheng, T. K. Dey, H. Edelsbrunner, M. A. Facello, and S. Teng. Sliver exudation. *Journal of the ACM*, 47, 2000.
- S. Cheng, T. K. Dey, and E. A. Ramos. Manifold reconstruction from point samples. In *Proceedings of the Symposium on Discrete Algorithms (SODA)*, 2005.
- S.-W. Cheng, T. K. Dey, and J. R. Shewchuk. *Delaunay Mesh Generation*. CRC Press, Boca Raton, Florida, Dec. 2012.

- F. Codevilla, M. Müller, A. Dosovitskiy, A. López, and V. Koltun. End-to-end driving via conditional imitation learning. In *ICRA*, 2018.
- C. Cortes and V. Vapnik. Support-vector networks. *Machine Learning*, 20, 1995.
- T. K. Dey. *Curve and Surface Reconstruction: Algorithms with Mathematical Analysis*. Cambridge University Press, 2007.
- T. K. Dey and S. Goswami. Provable surface reconstruction from noisy samples. In *Proceedings of the Symposium on Computational Geometry (SoCG)*, 2004.
- T. K. Dey and P. Kumar. A simple provable algorithm for curve reconstruction. In *Proceedings of the Symposium on Discrete Algorithms (SODA)*, 1999.
- T. K. Dey, J. Giesen, E. A. Ramos, and B. Sadri. Critical points of the distance to an epsilon-sampling of a surface and flow-complex-based surface reconstruction. In *Proceedings of the Symposium on Computational Geometry (SoCG)*, 2005.
- H. Edelsbrunner and N. R. Shah. Triangulating Topological Spaces. *International Journal of Computational Geometry and Applications*, Aug. 1997.
- G. F. Elsayed, D. Krishnan, H. Mobahi, K. Regan, and S. Bengio. Large margin deep networks for classification. *CoRR*, abs/1803.05598, 2018. URL <http://arxiv.org/abs/1803.05598>.
- A. Esteva, B. Kuprel, R. A. Novoa, J. Ko, S. M. Swetter, H. M. Blau, and S. Thrun. Dermatologist-level classification of skin cancer with deep neural networks. *Nature*, 2017.
- J. Franceschi, A. Fawzi, and O. Fawzi. Robustness of classifiers to uniform lp and gaussian noise. In *AISTATS*, 2018.
- J. Gilmer, L. Metz, F. Faghri, S. S. Schoenholz, M. Raghu, M. Wattenberg, and I. J. Goodfellow. Adversarial spheres. *CoRR*, abs/1801.02774, 2018. URL <http://arxiv.org/abs/1801.02774>.
- I. J. Goodfellow, J. Shlens, and C. Szegedy. Explaining and harnessing adversarial examples. In *ICLR*, 2014.
- M. Houry and J. R. Shewchuk. Fixed points of the restricted delaunay triangulation operator. In *Proceedings of the Symposium on Computational Geometry (SoCG)*, 2016.
- D. Kingma and J. Ba. Adam: A method for stochastic optimization. In *ICLR*, 2015.
- A. Krizhevsky, I. Sutskever, and G. E. Hinton. Imagenet classification with deep convolutional neural networks. In *NIPS*, 2012.
- A. Kurakin, I. Goodfellow, and S. Bengio. Adversarial examples in the physical world. In *ICLR Workshop Track*, 2016.
- S. Levine, N. Wagener, and P. Abbeel. Learning contact-rich manipulation skills with guided policy search. In *ICRA*, 2015.
- X. Liang, X. Wang, Z. Lei, S. Liao, and S. Z. Li. Soft-margin softmax for deep classification. In *ICONIP*, 2017.
- W. Liu, Y. Wen, Z. Yu, and M. Yang. Large-margin softmax loss for convolutional neural networks. In *ICML*, 2016.
- A. Madry, A. Makelov, L. Schmidt, D. Tsipras, and A. Vladu. Towards deep learning models resistant to adversarial attacks. In *ICLR*, 2018.
- N. Papernot, P. McDaniel, I. Goodfellow, S. Jha, Z. B. Celik, and A. Swami. Practical black-box attacks against machine learning. In *Proceedings of the Asia Conference on Computer and Communications Security*. ACM, 2017.
- N. Papernot, F. Faghri, N. Carlini, I. Goodfellow, R. Feinman, A. Kurakin, C. Xie, Y. Sharma, T. Brown, A. Roy, A. Matyasko, V. Behzadan, K. Hambardzumyan, Z. Zhang, Y.-L. Juang, Z. Li, R. Sheatsley, A. Garg, J. Uesato, W. Gierke, Y. Dong, D. Berthelot, P. Hendricks, J. Rauber, and R. Long. Technical report on the cleverhans v2.1.0 adversarial examples library. *arXiv preprint arXiv:1610.00768*, 2018.

- M. Raghu, B. Poole, J. M. Kleinberg, S. Ganguli, and J. Sohl-Dickstein. On the expressive power of deep neural networks. In *ICML*, 2017.
- A. Raghunathan, J. Steinhardt, and P. Liang. Certified defenses against adversarial examples. In *ICLR*, 2018.
- L. Schmidt, S. Santurkar, D. Tsipras, K. Talwar, and A. Madry. Adversarially robust generalization requires more data. In *NIPS*, 2018.
- L. Schott, J. Rauber, M. Bethge, and W. Brendel. Towards the first adversarially robust neural network model on MNIST. *CoRR*, abs/1805.09190, 2018. URL <https://arxiv.org/abs/1805.09190>.
- J. Shawe-Taylor and N. Cristianini. *Kernel Methods for Pattern Analysis*. Cambridge University Press, 2004.
- A. Sinha, H. Namkoong, and J. Duchi. Certifying some distributional robustness with principled adversarial training. In *ICLR*, 2018.
- D. Soudry, E. Hoffer, and N. Srebro. The implicit bias of gradient descent on separable data. In *ICLR*, 2018.
- S. Sun, W. Chen, L. Wang, X. Liu, and T.-Y. Liu. On the depth of deep neural networks: A theoretical view. In *AAAI*, 2016.
- C. Szegedy, W. Zaremba, I. Sutskever, J. Bruna, D. Erhan, I. J. Goodfellow, and R. Fergus. Intriguing properties of neural networks. *CoRR*, abs/1312.6199, 2013. URL <http://arxiv.org/abs/1312.6199>.
- Y. Wang, S. Jha, and K. Chaudhuri. Analyzing the robustness of nearest neighbors to adversarial examples. In *ICML*, 2018.
- A. C. Wilson, R. Roelofs, M. Stern, N. Srebro, and B. Recht. The marginal value of adaptive gradient methods in machine learning. In *NIPS*, 2017.
- E. Wong and J. Z. Kolter. Provable defenses against adversarial examples via the convex outer adversarial polytope. In *ICML*, 2018.
- Y. Wu, M. Schuster, Z. Chen, Q. V. Le, M. Norouzi, W. Macherey, M. Krikun, Y. Cao, Q. Gao, K. Macherey, J. Klingner, A. Shah, M. Johnson, X. Liu, L. Kaiser, S. Gouws, Y. Kato, T. Kudo, H. Kazawa, K. Stevens, G. Kurian, N. Patil, W. Wang, C. Young, J. Smith, J. Riesa, A. Rudnick, O. Vinyals, G. Corrado, M. Hughes, and J. Dean. Google’s neural machine translation system: Bridging the gap between human and machine translation. *CoRR*, abs/1609.08144, 2016. URL <http://arxiv.org/abs/1609.08144>.
- T. Zheng, C. Chen, and K. Ren. Distributionally adversarial attack. *CoRR*, abs/1808.05537, 2018. URL <http://arxiv.org/abs/1808.05537>.

A Auxiliary Results

Lemma 8. Let $\mathcal{M}_1, \mathcal{M}_2 \subset \mathbb{R}^d$ be k -dimensional manifolds such that $\mathcal{M} \cap \mathcal{M}_2 = \emptyset$. Let Λ_p be their decision axis for any $p > 0$ and let $\gamma : [0, 1] \rightarrow \mathbb{R}^d$ be any path such that $\gamma(0) \in \mathcal{M}_1$ and $\gamma(1) \in \mathcal{M}_2$. Then $\gamma \cap \Lambda \neq \emptyset$, that is γ must cross the decision axis.

Proof. Define $f_1, f_2 : [0, 1] \rightarrow \mathbb{R}$ as $f_1(t) = d(\gamma(t), \mathcal{M}_1)$ and $f_2(t) = d(\gamma(t), \mathcal{M}_2)$. Consider the function $g(t) = f_1(t) - f_2(t)$. Since $\mathcal{M}_1 \cap \mathcal{M}_2 = \emptyset$ and γ starts on \mathcal{M}_1 and terminates on \mathcal{M}_2 the function $g(0) < 0$ and $g(1) > 0$. Then, since g is continuous, the Intermediate Value Theorem implies that there exists $t_1 \in [0, 1]$ such that $g(t_1) = 0$. Thus $d(\gamma(t_1), \mathcal{M}_1) = d(\gamma(t_1), \mathcal{M}_2)$, which implies that $\gamma(t_1)$ is on the decision axis. \square

Theorem 9. Let f be any classifier on $\mathcal{M} = \mathcal{M}_1 \cup \mathcal{M}_2$. The maximum accuracy achievable, assuming a uniform distribution, on \mathcal{M}^ϵ is

$$1 - \frac{1}{2} \frac{\text{vol}(\mathcal{M}_1^\epsilon \cap \mathcal{M}_2^\epsilon)}{\text{vol}(\mathcal{M}_1^\epsilon \cup \mathcal{M}_2^\epsilon)}. \quad (11)$$

Proof. It is clearly optimal to classify points in $\text{vol}(\mathcal{M}_1^\epsilon \setminus \mathcal{M}_2^\epsilon)$ as class 1 and to classify points in $\text{vol}(\mathcal{M}_2^\epsilon \setminus \mathcal{M}_1^\epsilon)$ as class 2. Such a classifier can only be wrong when points lie in this intersection. For points in this intersection, the probability of a misclassification is $\frac{1}{2}$ for any classification that f makes. Thus, the probability of misclassification is

$$\frac{1}{2} \frac{\text{vol}(\mathcal{M}_1^\epsilon \cap \mathcal{M}_2^\epsilon)}{\text{vol}(\mathcal{M}_1^\epsilon \cup \mathcal{M}_2^\epsilon)}.$$

\square

Corollary 10. For $\epsilon < \text{rch}_p(\Lambda_p; \mathcal{M})$ there exists a decision boundary that correctly classifies \mathcal{M}^ϵ .

Proof. For $\epsilon < \text{rch}_p \Lambda_p$, $\mathcal{M}^\epsilon \cap \Lambda_p = \emptyset$ and so Λ_p is one such decision boundary. \square

B Additional Theoretical Results

A finite sample X of \mathcal{M} is said to exhibit Hausdorff noise up to τ if $X \subset \mathcal{M}^\tau$. That is every sample lies in a τ -tubular neighborhood of \mathcal{M} , not necessarily on \mathcal{M} . We can show a similar result to Theorem 3 for f_{nn} under moderate amounts of Hausdorff noise.

Theorem 11. Let X be a finite set sampled from \mathcal{M} such that $X \subset \mathcal{M}^\tau$ for some $\tau < \text{rch}_p \Lambda_p$; that is X lies near \mathcal{M} , in a τ -tubular neighborhood. If X is a δ -cover with $\delta \leq 2(\text{rch}_p \Lambda_p - \epsilon) - \tau$, then f_{nn} correctly classifies \mathcal{M}^ϵ .

Proof. Let $q \in \mathcal{M}_i^\epsilon$. The distance from q to any sampled in \mathcal{M}_j^ϵ for $j \neq i$ is lower bounded as $d(q, \mathcal{M}_j^\tau) \geq 2 \text{rch}_p \Lambda_p - \epsilon - \tau$. It is then both necessary and sufficient that there exists a sample $x \in \mathcal{M}_i^\tau$ such that $d(q, x) \leq 2 \text{rch}_p \Lambda_p - \epsilon - \tau$. The distance from q to the nearest sample in \mathcal{M}_i^τ is upper bounded by the δ -cover condition as $d(q, x) \leq \epsilon + \delta$. It suffices that

$$d(q, x) \leq \epsilon + \delta \leq 2 \text{rch}_p \Lambda_p - \epsilon - \tau \leq d(q, \mathcal{M}_j^\tau),$$

which implies that $\delta \leq 2(\text{rch}_p \Lambda_p - \epsilon) - \tau$. \square

Theorem 12. Let $z \in \mathcal{D}_{f_{\text{nn}}}$ be a point on the decision boundary of f_{nn} for a δ -cover X with $\delta < 1$. Let $\sigma \subset \mathcal{D}_{f_{\text{nn}}}$ be a linear facet of $\mathcal{D}_{f_{\text{nn}}}$ and note that σ is a Voronoi facet, let $\sigma^* = pq$ be the dual Delaunay edge of σ such that $p \in \mathcal{M}_1$ and $q \in \mathcal{M}_2$. Define $d(z, \mathcal{M}_1) = \omega_1 \text{rch}_2 \Lambda_2$ and $d(z, \mathcal{M}_2) = \omega_2 \text{rch}_2 \Lambda_2$, with $\omega_1 < \omega_2 < 1$. Then there exists a decision axis point $m \in \Lambda$ such that $d(z, m) \leq \frac{\delta^2 + (\omega_2^2 - \omega_1^2) + 2\delta\omega_2}{1 + (\omega_2^2 - \omega_1^2)} \omega_2 \text{rch}_2 \Lambda_2$.

Proof. If $z \in \Lambda_2$ then the result holds, so suppose that $z \notin \Lambda_2$.

The decision boundary $\mathcal{D}_{f_{\text{nn}}}$ is the union of a subset of $(d - 1)$ -dimensional Voronoi cells (along with their lower dimensional faces) of the Voronoi diagram $\text{Vor } X$ of X with the following property. For every Voronoi $(d - 1)$ -cell $\sigma \in \mathcal{D}_{f_{\text{nn}}}$, its dual Delaunay edge $\sigma^* = pq$ has endpoints $p, q \in X$ such that $p \in \mathcal{M}_1$ and $q \in \mathcal{M}_2$. That is, p and q have different class labels. In particular pq crosses Λ_2 . For every point $z \in \sigma$, $d(z, p) = d(z, q) \leq \min_i d(z, X_i)$; that is, p, q minimize the distance from z to any sample point in X . In the interior of σ this inequality is strict, while on the boundary of σ it may be realized by more points than just p and q . (See Appendix G for a brief review of Voronoi diagrams and Delaunay triangulations.)

Let $\sigma \in \mathcal{D}_{f_{\text{nn}}}$ be a Voronoi $(d-1)$ -cell that contains z and let $\sigma^* = pq$ be σ 's dual Delaunay edge. Imagine growing a ball B centered at z by increasing the radius r starting from 0. Due to the properties of Voronoi cells outlined above, the fact that $z \notin \Lambda_2$, and the fact that $X \subset \mathcal{M}$, the following three events occur in order as we increase r . First B intersects the manifold to which z is closest, without loss of generality \mathcal{M}_1 . Second B intersects \mathcal{M}_2 . Notice that at this point B has not intersected any sample points in X , since p and q are on \mathcal{M}_1 and \mathcal{M}_2 respectively and are the closest samples to z . Third B intersects p and q , when $r = d(z, p)$. Let r_1, r_2, r_3 denote the value of the radius at these three event points respectively. Similarly let B_1, B_2, B_3 denote the balls centered at z with radii r_1, r_2, r_3 respectively. Let $z_1 \in B_1 \cap \mathcal{M}_1$ and let $z_2 \in \mathcal{M}_2 \cap B_2$. Since \mathcal{M}_1 is the closer of the two manifolds to z , the line segment zz_2 must intersect Λ_2 . Let $\gamma : [0, 1] \rightarrow \mathbb{R}^d$ parameterize the line segment zz_2 , where $\gamma(0) = z$, $\gamma(1) = z_2$, and $\|z - \gamma(t)\|_2 = r_2 t$. We will show that there exists a decision axis point $m \in \gamma$ that is close to z .

The ball B_2 is tangent to \mathcal{M}_2 at z_2 but contains some portion of \mathcal{M}_1 . Our approach will be to move the center of B_2 along γ from z to z_2 while maintaining tangency at z_2 . That is we consider the balls $B_t = B(\gamma(t), \|\gamma(t) - z_2\|_2)$ as t increase from 0 to 1. For some t^* , $B_{t^*} \cap \mathcal{M}_1 = \emptyset$ which means that we have crossed the decision axis. We will prove that t^* must be small which implies that $\|z - m\|_2 \leq \|z - \gamma(t^*)\|_2 \leq r_2 t^*$ is small.

We begin by considering the triangle $\Delta z_1 z z_2$. Using the law of cosines we derive an expression for the angle $\angle z_1 z z_2$ as

$$\begin{aligned} \|z_1 - z_2\|_2^2 &= r_1^2 + r_2^2 - 2r_1 r_2 \cos \angle z_1 z z_2 \\ \cos \angle z_1 z z_2 &= \frac{r_1^2 + r_2^2 - \|z_1 - z_2\|_2^2}{2r_1 r_2}. \end{aligned}$$

As t increases the event $B_t \cap \mathcal{M}_1 = \emptyset$ occurs when the distances from $\gamma(t)$ to any point $x \in B_2 \cap \mathcal{M}_1$ is greater than $r_2(1-t)$. Due to the δ -cover condition at z_1 and the fact that $B_2 \subset B_3$ where B_3 is the event where a ball centered at z intersects a sample point, every such x must lie in a ball $B(z_1, g)$ for $g \leq \delta$. Thus the event $B_t \cap \mathcal{M}_1 = \emptyset$ occurs for the minimum t such that

$$\begin{aligned} \|z_1 - \gamma(t)\|_2 - g &\geq r_2(1-t) \\ \|z_1 - \gamma(t)\|_2^2 &\geq r_2^2(1-t)^2 + 2gr_2(1-t) + g^2. \end{aligned}$$

First we derive an expression for $\|z_1 - \gamma(t)\|_2$ again using the law of cosines and substituting the expression for $\angle z_1 z z_2$.

$$\begin{aligned} \|z_1 - \gamma(t)\|_2^2 &= r_1^2 + r_2^2 t^2 - 2r_1 r_2 t \cos \angle z_1 z z_2 \\ &= r_1^2 + r_2^2 t^2 - t(r_1^2 + r_2^2 - \|z_1 - z_2\|_2^2) \\ &= (1-t)r_1^2 + (t-1)tr_2^2 + t\|z_1 - z_2\|_2^2. \end{aligned}$$

So then $\|z_1 - \gamma(t)\|_2^2 \geq r_2^2(1-t)^2 + 2gr_2(1-t) + g^2$ holds if and only if

$$\begin{aligned} (1-t)r_1^2 + (t-1)tr_2^2 + t\|z_1 - z_2\|_2^2 &\geq r_2^2(1-t)^2 + 2gr_2(1-t) + g^2 \\ t &\leq \frac{g^2 - r_1^2 + 2gr_2 + r_2^2}{\|z_1 - z_2\|_2^2 - r_1^2 + 2gr_2 + r_2^2} \\ &\leq \frac{g^2 - r_1^2 + 2gr_2 + r_2^2}{\|z_1 - z_2\|_2^2 - r_1^2 + r_2^2} \\ &\leq \frac{\delta^2 + (\omega_2^2 - \omega_1^2) + 2\delta\omega_2}{1 + (\omega^2 - \omega_1^2)} \end{aligned}$$

□

C Additional Experiments

We present additional experiments to support our theoretical predictions. We reproduce the results of Section 8 using different optimization algorithms (Section C.1) and attack methods (Section C.2). These additional experiments are consistent with our conclusions in Section 8.

C.1 Reproducing Results using SGD

In Section 8.1 we showed that increasing the codimension reduces the robustness of the decision boundaries learned by Adam on CIRCLES. In Figure 15 we reproduce this result using SGD. Again we see that as we increase the codimension the robustness decreases. SGD presents with much less variances than Adam, which we attribute to implicit regularization that has been observed for SGD (Soudry et al. (2018))

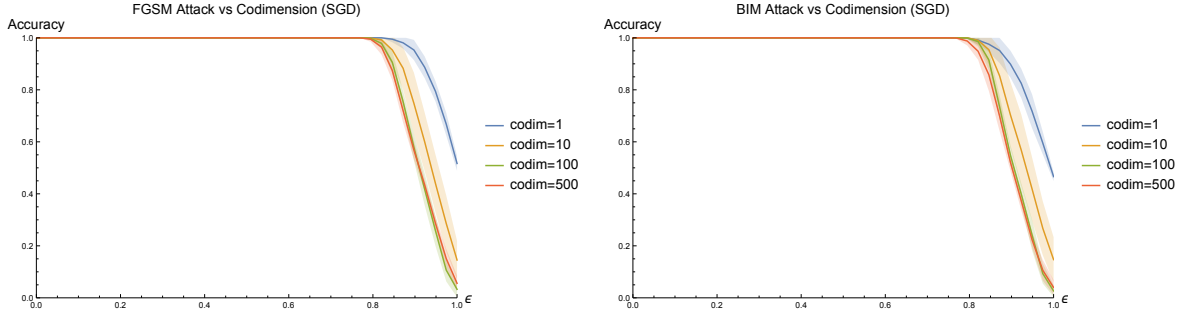


Figure 15: As in the case of training with Adam, we see a steady decrease in robustness on the CIRCLES dataset as the codimension increases when training with SGD.

Next we consider the adversarial training procedure of Madry et al. (2018) using SGD instead of Adam. We note that the authors of Madry et al. (2018) use Adam in their own experiments. Figure 16 shows that the result is consistent with the result in Section 8.1. Again SGD presents with lower variance.

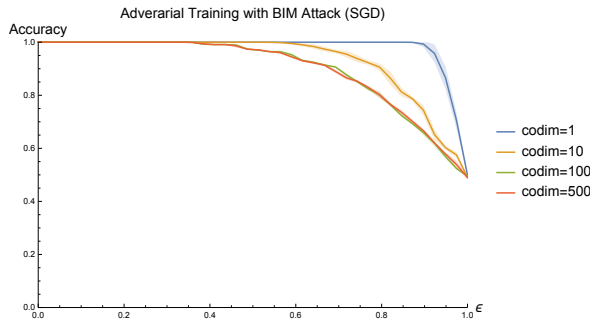


Figure 16: Adverarial training with a PGD adversary, as in Figure 9, using SGD. Similarly we see a drop in robustness as the codimension increases.

C.2 Reproducing Results using FGSM

In Section 8.1 we evaluated the robustness of nearest neighbors against BIM attacks under the $\|\cdot\|_\infty$ on MNIST. In Figure 17 we evaluate the robustness of nearest neighbors against FGSM attacks under the $\|\cdot\|_\infty$ on MNIST. We use the naturally pretrained (natural) and adversarially pretrained (robust) convolutional models provided by Madry et al. (2018)¹. Figure 17 (Left) shows that nearest neighbors is substantially more robust to FGSM attacks than the naturally trained model. Figure 17 (Right) shows that nearest neighbors is comparable to the robust model up to $\epsilon = 0.3$, which is the value for which the robust model was trained. After $\epsilon = 0.3$, nearest neighbors is substantially more robust to FGSM attacks than the robust model. At $\epsilon = 0.5$, nearest neighbors maintains accuracy of 78% to adversarial perturbations that cause the accuracy of the robust model to drop to 39%.

D The Madry Defense Suffers from Obfuscated Gradients

Athalye et al. (2018) identified the problem of “obfuscated gradients”, a type of a gradient masking (Papernot et al. (2017)) that many proposed defenses employed to defend against adversarial examples. They identified three different types of obfuscated gradients: shattered gradients, stochastic gradients, and exploding/vanishing

¹https://github.com/MadryLab/mnist_challenge

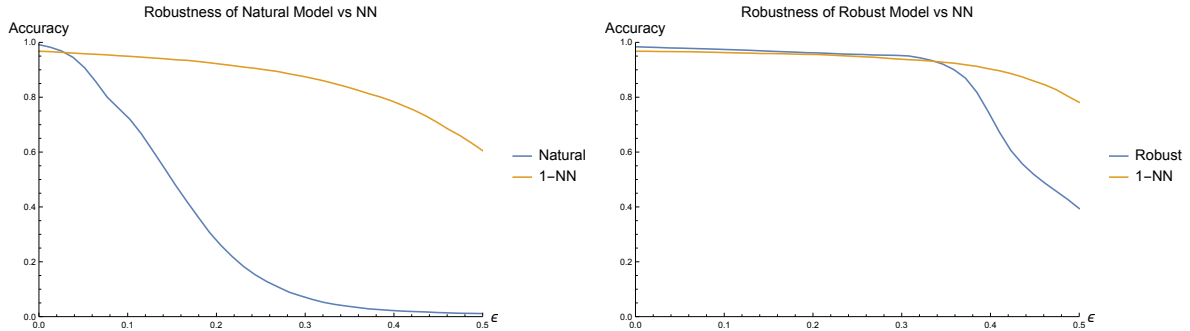


Figure 17: Robustness of nearest neighbors against the naturally trained (left) and adversarially trained (right) convolutional models of Madry et al. (2018) against FGSM attacks under the $\|\cdot\|_\infty$ norm on MNIST.

gradients. They examined nine recently proposed defenses, concluded that seven suffered from at least one type of obfuscated gradient, and showed how to circumvent each type of obfuscated gradient and thus each defense that employed obfuscated gradients.

Regarding the work of Madry et al. (2018), Athalye et al. (2018) stated “We believe this approach does not cause obfuscated gradients”. They note that “our experiments with optimization based attacks do succeed with some probability”. In this section we provide evidence that the defense of Madry et al. (2018) *does* suffer from obfuscated gradients, specifically shattered gradients. Shattered gradients occur when a defence causes the gradient field to be “nonexistent or incorrect” (Athalye et al. (2018)). Specifically we provide evidence that the defense of Madry et al. (2018) works by shattering the gradient field of the loss function around the data manifolds.

In Figure 18 (Left) we show the normalized gradient field of the loss function for a network trained on a 2-dimensional version of our PLANES dataset using the adversarial training procedure of Madry et al. (2018) with a PGD adversary. While the gradients have meaningful directions, Figure 18 (Left) shows that magnitude of the gradient field is nearly 0 everywhere around the data manifolds, which are at $y = 0$ and $y = 2$. The only notable gradients are near the decision axis which is at $y = 1$.

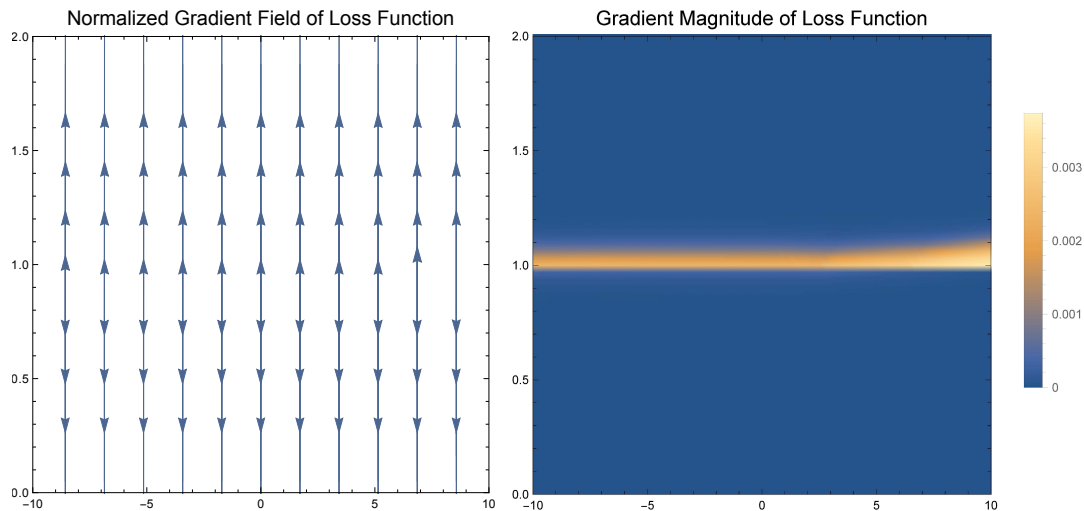


Figure 18: (Left) The normalized gradient field of the loss for an adversarially trained network. (Right) The magnitudes of the gradient. Notice that the gradients are largely 0 except at the decision axis $y = 1$.

One criteria that Athalye et al. (2018) propose for identifying obfuscated gradients is whether one-step attacks perform better than iterative attacks. The reason this criteria is useful for identifying obfuscated gradients is because one-step attacks like FGSM first normalize the gradient, ignoring its magnitude, then take as large of a step as allowed in the direction of the normalized gradient. So long as the gradient *on the manifold* points towards the decision boundary, FGSM will be effective at finding an adversarial example.

In Figure 19 we show the adversarial examples generated using PGD (left), FGSM (center), and BIM (right) for $\epsilon = 1$ starting at the test set for the PLANES dataset. FGSM produces adversarial examples at the decision

axis $y = 1$, exactly where we would expect. Notice that all of the adversarial perturbation is normal to the data manifold, suggesting that the gradient on the manifold points towards the decision boundary. However the adversarial examples produced by PGD lie closer to the manifold from which the example was generated.

PGD splits the total perturbation between both the normal and the tangent spaces of the data manifold, as shown by the arrows in Figure 19. This suggests that, when trained adversarially, the network learned a gradient field that has small but correct gradients on the data manifold, but gradients that curve in the tangent directions immediately *off the manifold*.

Lastly notice that BIM, another iterative method, also produces adversarial examples that are near the decision axis. Athalye et al. (2018) cite success with iterative based optimization procedures as evidence against obfuscated gradients. However BIM also ignores the magnitude of the gradient, as it simply applies FGSM iteratively. The network has learned a gradient field that is overfit to the particulars of the PGD attack. BIM successfully navigates this gradient field, while PGD does not. While the network is robust to PGD attacks at test time, it is less robust to FGSM and BIM attacks.

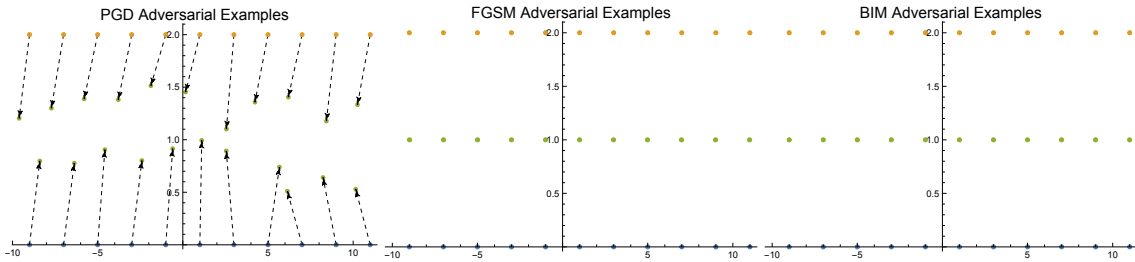


Figure 19: Adversarial examples generated using PGD (left), FGSM (center), and BIM (right). While the network is robust to PGD attacks, FGSM and BIM attacks are more effective because they ignore the magnitude of the gradient. For PGD we draw arrows from the test sample to the adversarial example generated from that point to aid the reader.

E Implementation Details

For the iterative attacks BIM and PGD, we set the number of iterations to 30 with a step size of $\epsilon_{\text{step}} = 0.05$ per iteration.

Our controlled experiments on synthetic data consider a fully connected network with 1 hidden layer, 100 hidden units, and ReLU activations. This model architecture is more than capable of representing a nearly perfect robust decision boundary for both CIRCLES and PLANES, the latter of which is linearly separable. We set the learning rate for Adam as $\alpha = 0.1$, which we found to work best for our datasets. The parameters for the exponential decay of the first and second moment estimates were set to $\beta_1 = 0.9$ and $\beta_2 = 0.999$. We set the learning rate for SGD as $\alpha = 0.1$ and decrease the learning rate by a factor of 10 every 100 epochs. We train all of our models for 250 epochs, following Wilson et al. (2017). We train using a cross-entropy loss.

All of our experiments are implemented using PyTorch. When comparing against a published result we use publicly available repositories, if able. For the robust loss of Wong and Kolter (2018), we use the code provided by the authors². The provided implementation³ of the adversarial training procedure of Madry et al. (2018) considers a PGD adversary with $\|\cdot\|_{\infty}$ -perturbations. We reimplemented their adversarial training procedure for $\|\cdot\|_2$ -perturbations following their implementation and using the PGD attack implemented in the cleverhans library (Papernot et al. (2018)).

The models of Madry et al. (2018) consist of two convolutional layers with 32 and 64 filters respectively, each followed by 2×2 max pooling. After the two convolutional layers, there are two fully connected layers each with 1024 hidden units.

²https://github.com/locuslab/convex_adversarial

³https://github.com/MadryLab/mnist_challenge

F Volume Arguments for d -Spheres

Let $S \subset \mathbb{R}^{d+1}$ be a unit d -sphere embedded in \mathbb{R}^{d+1} . The volume of S^ϵ is given by

$$\text{vol } S^\epsilon = \frac{\pi^{d/2}((1+\epsilon)^d - (1-\epsilon)^d)}{\Gamma(1 + \frac{d}{2})}, \quad (12)$$

where Γ denotes the gamma function. Let $X \subset S$ be a finite sample of size n of S . The set X^ϵ is the set of all ϵ perturbations of points in X under the norm $\|\cdot\|_2$. How well does X^ϵ approximate S^ϵ as a function of n , d and ϵ ?

To answer this question we upper bound the ratio $\text{vol } X^\epsilon / \text{vol } S^\epsilon$ by generously assuming that the balls $B(X_i, \epsilon)$ are disjoint. The resulting upper bound is

$$\frac{\text{vol } X^\epsilon}{\text{vol } S^\epsilon} \leq \frac{n \text{vol } B_\epsilon}{\text{vol } S^\epsilon} = \frac{n\epsilon^d}{(1+\epsilon)^d - (1-\epsilon)^d}. \quad (13)$$

In Figure 20 we show three different views of this bound. In Figure 20 (Left) we set $n = 10^{12}$ and plot four different values of ϵ ; in each case the percentage of volume of S^ϵ that is covered by X^ϵ quickly approaches 0. Similarly, in Figure 20 (Center), if we fix $\epsilon = 1$ and plot four different values of n , in each case we have the same result. Finally in Figure 20 (Right) we plot a lower bound on number of samples necessary to cover S^ϵ by X^ϵ for four different values of ϵ ; in each case the number of samples necessary grows exponentially with the dimension.

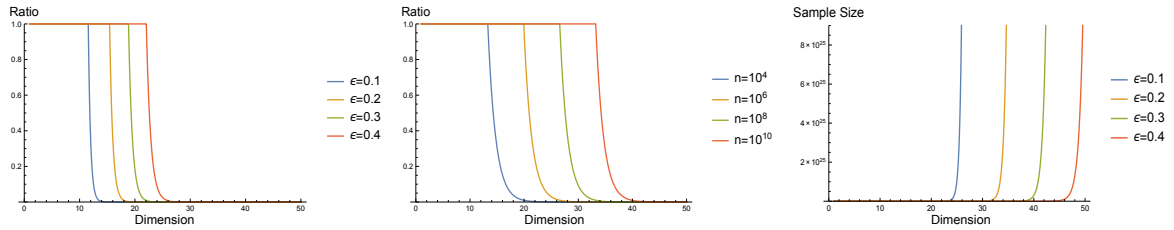


Figure 20: Three different perspectives on our upper bound in Equation 13. (Left, Center) In each case the percentage of S^ϵ covered by X^ϵ goes to 0. (Right) The number of points necessary to cover S^ϵ by X^ϵ grows exponentially with the dimension.

G Voronoi Diagrams and Delaunay Triangulations

Let $X \subset \mathbb{R}^d$ be a finite set of n points. The *Voronoi diagram* of X , denoted $\text{Vor } X$, under the metric $d(\cdot, \cdot)$ is a subdivision of \mathbb{R}^d into n cells where each cell is defined as

$$\text{Vor } v = \{x \in \mathbb{R}^d : d(x, v) \leq d(x, u), \forall u \in X \setminus \{v\}\}. \quad (14)$$

In words, the Voronoi cell $\text{Vor } v$ of $v \in X$ is the set of all points in \mathbb{R}^d that are closer to v than any other sample point $u \neq v$ in X . The Voronoi diagram is then defined as the set of all Voronoi cells, $\text{Vor } X = \{\text{Vor } v : v \in X\}$. When $d(\cdot, \cdot)$ is induced by the norm $\|\cdot\|_2$, the Voronoi cells are convex. See Figure 21.

The *Delaunay triangulation* of X , denoted $\text{Del } X$ is a triangulation of the convex hull of X into d -simplices. Every d -simplex $\tau \in \text{Del } X$, as well as every lower-dimensional face of τ , has the defining property that there exists an empty circumscribing ball B such that the vertices of τ lie on the boundary of B and the interior of B is free from any points in X . See Figure 21. This *empty circumscribing ball* property of Delaunay triangulations implies many desirable properties that are useful in mesh generation (Cheng et al. (2012)) and manifold reconstruction (Edelsbrunner and Shah (1997)). The Delaunay triangulation of a point set always exists, but is not unique in general.

There exists a well known *duality* between the Voronoi diagram and the Delaunay triangulation of X . For every j -dimensional face $\sigma \in \text{Vor } X$ there exist a dual $(d-j)$ -dimensional simplex denoted $\sigma^* \in \text{Del } X$ whose $d-j+1$ vertices are the $d-j+1$ vertices of X whose Voronoi cells intersect at σ . In particular, every d -cell of $\text{Vor } X$ is dual to the vertex of $\text{Del } X$ that generates that cell, and every $(d-1)$ -face of $\text{Vor } X$ is dual to an edge of $\text{Del } X$.

A nearest neighbor classifier f_{nn} given a query point q simply returns the class of the point in X that generated the Voronoi cell in which q lies. Thus the decision boundary of f_{nn} is the union of $(d-1)$ and lower dimensional Voronoi faces. Furthermore, when X is a dense sample of a manifold \mathcal{M} , the Voronoi cells are well known to be elongated in the directions normal to \mathcal{M} Dey (2007). This fact underlies many of our results.

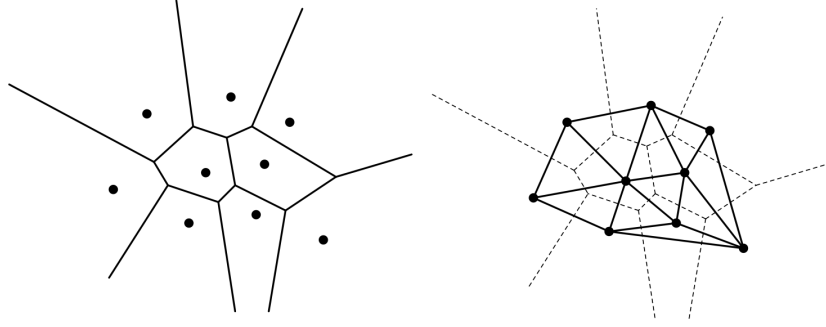
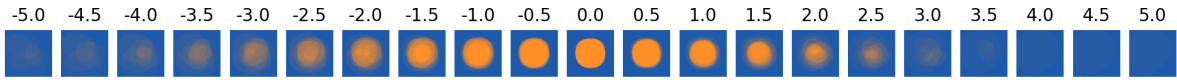


Figure 21: The Voronoi diagram of a set of points in \mathbb{R}^2 (left) and its dual the Delaunay triangulation (right).

H Visualization of Decision Boundaries

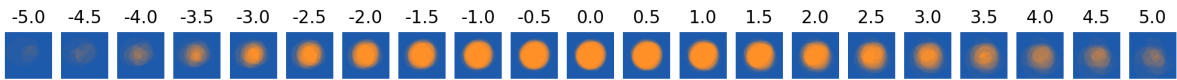
In Figure 22 we provide visualizations of the decision boundaries learned by (a-d) our fully connected network architecture with cross entropy loss for various optimization procedures and various training lengths, and (e) a nearest neighbor classifier for $\|\cdot\|_2$ on the training set. Specifically we train on the CIRCLES dataset, embedded in \mathbb{R}^3 . The training set is entirely contained in the xy -plane. We then visualize cross sections of the decision boundary for various values of $z \in [-5, 5]$. We color points labeled as in the same class as the outer circle with the color blue and points labeled as in the same class as the inner circle as orange. Figure 22 shows the cross sections of the decision boundaries, averaged over 20 retrainings. The visualization shows how various optimization algorithms learn decision boundaries that extend into the normal directions where no data is provided.



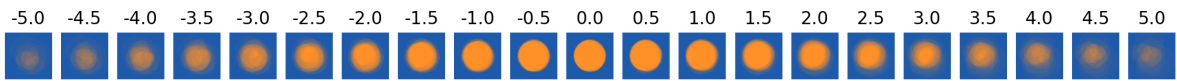
(a) Decision boundary learned by running SGD for 25 epochs, averaged over 20 trainings.



(b) Decision boundary learned by running SGD for 250 epochs, averaged over 20 trainings.



(c) Decision boundary learned by running Adam for 25 epochs, averaged over 20 trainings.



(d) Decision boundary learned by running Adam for 250 epochs, averaged over 20 trainings.



(e) Decision boundary of a nearest neighbor classifier for the $\|\cdot\|_2$ norm.

Figure 22: The training set lies entirely in the xy -plane, shown here at $z = 0$. We visualize cross sections of the decision boundary for $z \in [-5, 5]$ for various optimization algorithms training for different lengths of time. The results show how various optimization algorithm learn decision boundaries that extend into the normal directions in which there is no data provided. We average the decision boundary over 20 retrainings, so faded results indicate how frequently a point was labeled a specific class.